

Integrating high-quality dielectrics with one-nanometer equivalent oxide thickness on two-dimensional electronic devices

Weisheng Li^{1,†}, Jian Zhou^{1,†}, Songhua Cai^{2,†}, Zhihao Yu¹, Jialin Zhang³, Nan Fang⁴, Taotao Li², Yun Wu⁵, Tangsheng Chen⁵, Xiaoyu Xie⁶, Haibo Ma⁶, Ke Yan¹, Ningxuan Dai¹, Xiangjin Wu¹, Huijuan Zhao¹, Zixuan Wang¹, Daowei He^{1,7}, Lijia Pan¹, Yi Shi¹, Peng Wang^{2,*}, Wei Chen³, Kosuke Nagashio⁴, Xiangfeng Duan⁷ & Xinran Wang^{1,*}

¹*National Laboratory of Solid State Microstructures, School of Electronic Science and Engineering and Collaborative Innovation Center of Advanced Microstructures, Nanjing University, Nanjing 210093, China*

²*National Laboratory of Solid State Microstructures, Jiangsu Key Laboratory of Artificial Functional Materials, College of Engineering and Applied Sciences and Collaborative Innovation Center of Advanced Microstructures, Nanjing University, Nanjing 210093, China*

³*Department of Chemistry, National University of Singapore, 3 Science Drive 3, 117543, Singapore*

⁴*Department of Materials Engineering, The University of Tokyo, Tokyo 113-8656, Japan*

⁵*Science and Technology on Monolithic Integrated Circuits and Modules Laboratory, Nanjing Electronic Device Institute, Nanjing 210016, China*

⁶*School of Chemistry and Chemical Engineering, Nanjing University, Nanjing 210023, China*

⁷*Department of Chemistry and Biochemistry, University of California, Los Angeles, CA, USA.*

† These authors contribute equally to this work.

* Corresponding authors: xrwang@nju.edu.cn, wangpeng@nju.edu.cn

Two-dimensional (2D) semiconductors are widely recognized as attractive channel materials for low-power electronics. However, an unresolved challenge is the integration of high-quality, ultrathin high- κ dielectrics that fully meet the roadmap requirements for low-power applications. With a dangling-bond free surface, the deposition of dielectrics by atomic layer deposition (ALD) on 2D materials is usually characterized with non-uniform nucleation and island formation, producing a highly porous dielectric layer with serious leakage particularly at the small equivalent oxide thickness (EOT) limit. Here, we report the robust ALD of highly uniform high- κ dielectric on 2D semiconductors by using

~0.3 nm-thick exclusively monolayer molecular crystal as seeding layer. Ultrathin dielectrics down to 1 nm EOT is realized on graphene, MoS₂ and WSe₂, with considerably reduced roughness, density of interface states, leakage current and improved breakdown field compared to prior methods. Taking advantage of the reduced EOT, we demonstrate graphene RF transistors operating at 60 GHz, as well as MoS₂ and WSe₂ complementary metal-oxide-semiconductor (CMOS) transistors with $V_{dd}=0.8$ V and ideal subthreshold swing (SS) of 60 mV/dec, 20 nm-channel-length MoS₂ transistors with on/off ratio over 10⁷. These studies highlight that our dielectric integration method is generally applicable for different 2D materials, and compatible with top-down fabrication process on large-area chemical vapor deposited films.

The ever-growing demand for portable electronics requires continuous development of energy-efficient logic devices. In Si CMOS technology, scaling under constrained thermal budget is made possible by the continuous reduction of EOT and the supply voltage (V_{dd}) on single transistor level¹. Currently in the most advanced Si metal-oxide-semiconductor field-effect transistors (MOSFETs) (e.g. Intel 14 nm FinFET structure), the physical thickness of HfO₂ is 2.6 nm, corresponding to 0.9 nm EOT². In addition, the gate leakage and interface state density (D_{it}) required for low-standby-power CMOS³ is 1.5×10^{-2} A/cm² and $\sim 10^{10}$ cm⁻²eV⁻¹. These numbers serve as important benchmarks for any emerging technologies.

To further mitigate SCE in ultra-scaled MOSFET, an alternative route is to reduce the channel thickness, as the characteristic length to avoid SCE scales with $\sqrt{\frac{\epsilon_{ch}}{N\epsilon_{ox}} t_{ch} t_{ox}}$. Here, t_{ch} (ϵ_{ch}) and t_{ox} (ϵ_{ox}) are thickness (dielectric constant) of channel and gate oxide, N is the number of gate⁴. Therefore, 2D semiconductors, in particular large bandgap transition-metal dichalcogenides (TMDs), have been extensively studied as promising channel materials for low-power electronics⁴⁻⁷. However, to integrate high- κ gate dielectric on 2D materials, with sub-1 nm EOT and equivalent leakage current and interface quality as Si CMOS, represents a standing challenge, largely due to difficulties in uniformly nucleates on the intrinsically dangling-bond-free surface of most 2D materials. The ALD deposition on 2D materials was usually achieved through chance nucleation at defects, edges and impurities to produce highly porous thin films⁴⁻⁷. Over the past decade, many interfacial activation layers/processes have been developed for uniform deposition of high- κ oxides on 2D materials⁸, such as oxidized metal layer⁹, organic molecules¹⁰⁻¹³, BN¹⁴, ozone¹⁵, mild plasma treatment¹⁶, and electron beam

irradiation¹⁷. However, all these methods have their own drawbacks. For examples, the widely used metal oxidation process suffer from inherent roughness of evaporated metal films as well as damages by high-energy metal ions¹⁸. Ozone/plasma/electron irradiation processes also involve high-energy and reactive species which can introduce defects and interface states. For molecular layers, it is still difficult to achieve defect-free and precise thickness control over the entire device area¹⁹. Although exfoliated BN has been proven as an ideal dielectric for 2D materials²⁰, the leakage current is much higher than the requirement by International Technology Roadmap for Semiconductors (ITRS) due to its low dielectric constant²⁰, and the aligned transfer process is unscalable. So far, the smallest EOT reported on graphene and TMDs is 1.3 nm and 2.5 nm, respectively^{17, 21}. The trade-off between EOT, interface quality and scalability has not been resolved. A transfer gate process has also been explored for integrating high quality gate dielectrics on 2D materials, although it usually involve unusual soft-lithography process and is not readily compatible with current semiconductor manufacturing²²⁻²⁴.

For low-power logic applications, the requirements of the interfacial buffer layer on 2D materials are extremely stringent. First, the thickness has to approach single atomic layer because any additional thickness would reduce the gate capacitance and make ~ 1 nm EOT almost impossible. Second, it has to be closely packed on nanometer scale and uniform on micrometer scale to avoid pinholes in the gate dielectric. Third, the interaction should be non-covalent to preserve the intrinsic properties of 2D materials and interfaces, preferably to the level of BN/2D. Finally, the process needs to be robust and scalable to large-area chemical vapor deposition (CVD) films. In this work, we develop a technique to integrate ultrathin high- κ dielectric on graphene, BN and TMDs that satisfies the above requirements simultaneously. We use 3,4,9,10-perylene-tetracarboxylic dianhydride (PTCDA) molecular crystal non-covalently bound to 2D materials as the seeding layer for ALD. The thickness can be controlled precisely to monolayer (ML, ~ 0.3 nm) using self-limited epitaxy²⁵, which is a major advancement over prior works^{12, 19}. We achieve record-low EOT=1 nm ($t_{ox}=1.45$ nm) on graphene and MoS₂ without sacrificing the dielectric properties. Notably, the PTCDA/HfO₂ gate dielectric show low leakage current $J < 10^{-2}$ A/cm² and high breakdown field $E_{bd}=16.5$ MV/cm at 1 nm EOT, which are considerably better than other approaches on 2D materials and meet the ITRS requirement for low-power devices. We also achieve the lowest D_{it} among top-gate MoS₂ FETs by ALD. Owing to the low EOT and D_{it} , we are able to reduce the V_{dd} of TMD CMOS to the state-of-the-art Si CMOS, with on/off $> 10^6$ and nearly ideal switching behavior.

We further demonstrate 20 nm-short-channel MoS₂ transistors with on/off >10⁷ and SS=73 mV/dec. Finally, we grow ML PTCDA/HfO₂ on large-area CVD MoS₂ films and fabricate top-down transistor arrays with excellent yield and reproducibility. Our technology truly enables the potential of 2D materials for low-power logic applications.

Deposition of high- κ dielectrics on 2D materials using ML PTCDA as seeding layer

Fig. 1a illustrates the HfO₂/ML PTCDA/2D material hybrid structure studied in this work. PTCDA is well known to have a layered crystal structure, with 0.3 nm interlayer distance corresponding to the π - π stack direction (Supplementary Fig. S1). When grown on 2D surfaces like graphene, it self-assembles into a herringbone lattice stabilized by hydrogen bonding²⁶. To obtain ultrathin EOT, controllable growth of exclusively ML PTCDA seeding layer is crucial. We carried out self-limited van der Waals epitaxial growth in a tube furnace described by our previous work²⁵. The ML PTCDA film was highly crystalline and uniform as confirmed by atomic force microscopy (AFM) (Fig. 1c, Supplementary Fig. S1), cross-polarized optical microscopy (Supplementary Fig. S2) and scanning tunneling microscopy (STM) (Fig. 1a inset). High-resolution STM clearly revealed herringbone packing, consistent with previous experiments²⁶ and theoretical calculations²⁷. The self-limited growth could be understood by the thickness-dependent binding energy calculated by molecular dynamics simulations (Fig. 1b). For graphene and BN, the binding energy on substrate is higher than that on additional PTCDA layers due to strong π - π interaction, indicating that the first layer is thermodynamically more stable. Although the trend was opposite on MoS₂, we were still able to grow uniform ML as shown by the height increase of 0.3-0.4 nm in AFM (Fig. 1d, Supplementary Fig. S1) and scanning transmission electron microscopy (STEM) (Fig. 2).

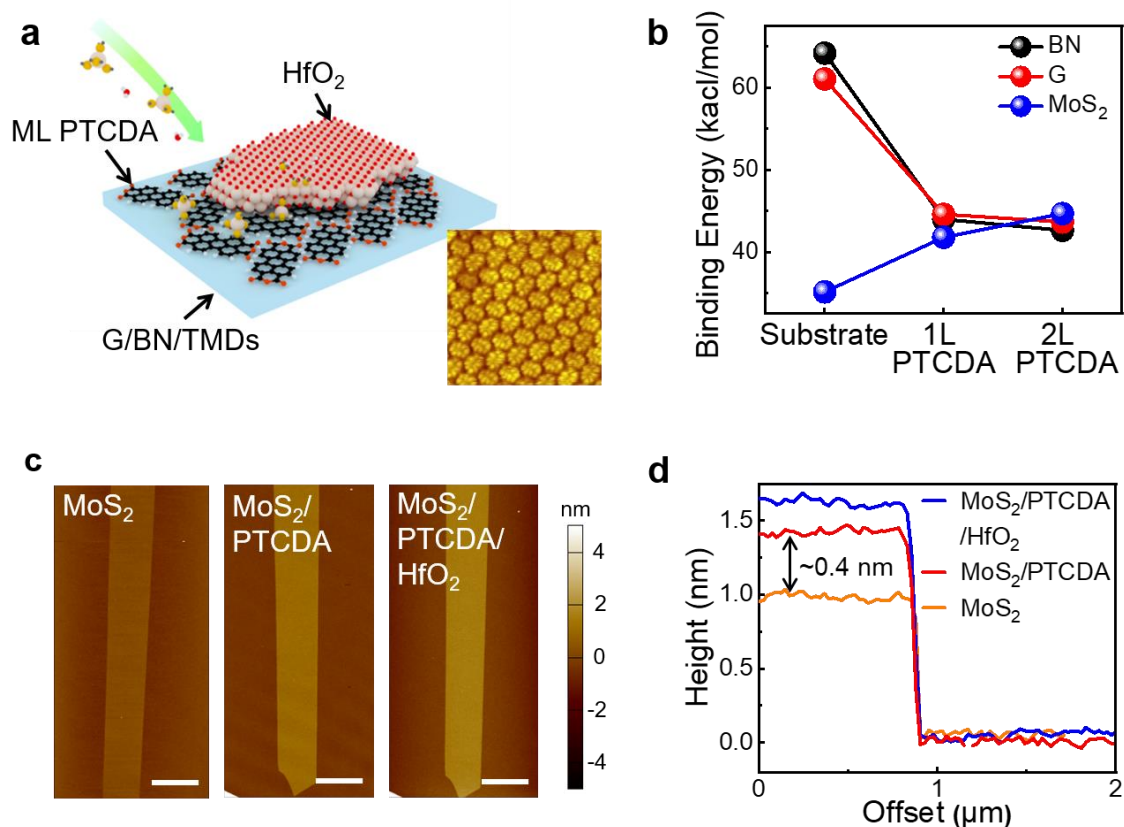


Figure 1. Deposition of ultrathin high-k oxide on 2D materials. **a.** Schematic illustration of the hybrid ML PTCDA/HfO₂ gate stack on 2D materials. Inset shows a 10 nm×10 nm high-resolution STM scan of ML PTCDA on graphene. **b.** Calculated PTCDA-substrate binding energy on different 2D materials. **c.** AFM images of an exfoliated MoS₂ (left), after ML PTCDA deposition (middle) and after 2 nm HfO₂ deposition (right). Scale bars are 3 μm. **d.** Height profile measured from **c**.

Following adsorption on 2D materials, the carbonyl functional groups in PTCDA molecules serve as closely distributed sites for ALD nucleation. Indeed, graphene became more hydrophilic after ML PTCDA deposition, with water contact angle decreased from 95 ° to 62 ° (Supplementary Fig. S3). The large binding energy stabilized the PTCDA layer at our ALD temperature of 150 °C as confirmed by Raman spectroscopy (Supplementary Fig. S4). As a result, we were able to deposit pinhole-free HfO₂ on graphene, BN and TMDs (including MoS₂, WS₂, MoSe₂ and WSe₂) with extremely low mean-square roughness of 0.13 nm (Fig.

1c, d, Supplementary Fig. S1). The roughness is the lowest on 2D materials so far (Table S1), proving that ML PTCDA crystal is an excellent seeding layer. As expected, the control samples without PTCDA showed discontinuous oxide deposition (Supplementary Fig. S1).

The pristine quality of the dielectric interface was further revealed by STEM (Fig. 2, Supplementary Fig. S5). Fig. 2a-c are bright-field cross-section STEM images of ML PTCDA/HfO₂ dielectric stack on graphene, BN and MoS₂, respectively, showing very smooth HfO₂ down to 2 nm. It is worth mentioning that the same uniformity was maintained over the entire device area of several micrometers consistent with AFM (see the white horizontal line in the low magnification image in Supplementary Fig. S5a). The ML PTCDA was clearly observed as an additional layer above graphene and BN (Fig. 2a, b), with an interlayer distance of ~0.31 nm corresponding to the van der Waals gap. The PTCDA layer was rougher than the topmost layer of 2D materials, possibly due to the damage by focus ion beam during sample preparation. The PTCDA layer appeared as a bright straight line on MoS₂ because Mo and S elements are much heavier than C (Fig. 2c). To verify the elemental distribution and existence of PTCDA on MoS₂, STEM-EELS mapping was carried out in this region. By extracting the signals of S, O and C edges in EELS spectrum from every scanning pixel, the distribution of these elements was mapped out (Fig. 2d), and corresponding well to the device structure. We clearly observed a high concentration of C signal at the HfO₂/MoS₂ interface. Close inspection of the EELS spectrum revealed that the main C peak was red-shifted compared to amorphous C contaminations from other positions (Fig. 2e), due to the existence of C=O bond in PTCDA²⁸. The same trend was followed in the case of PTCDA on BN (Fig. S5d), proving unequivocally that ML PTCDA served as the seeding layer. To compare with other growth methods, we also performed STEM characterizations on a control sample with 1 nm evaporated Al buffer layer and 4 nm HfO₂ (Supplementary Fig. S5c), which shows damage of 2D material as well as fluctuation of oxide thickness by 0.6 nm. The quality of stack is clearly inferior to our PTCDA/HfO₂ stack.

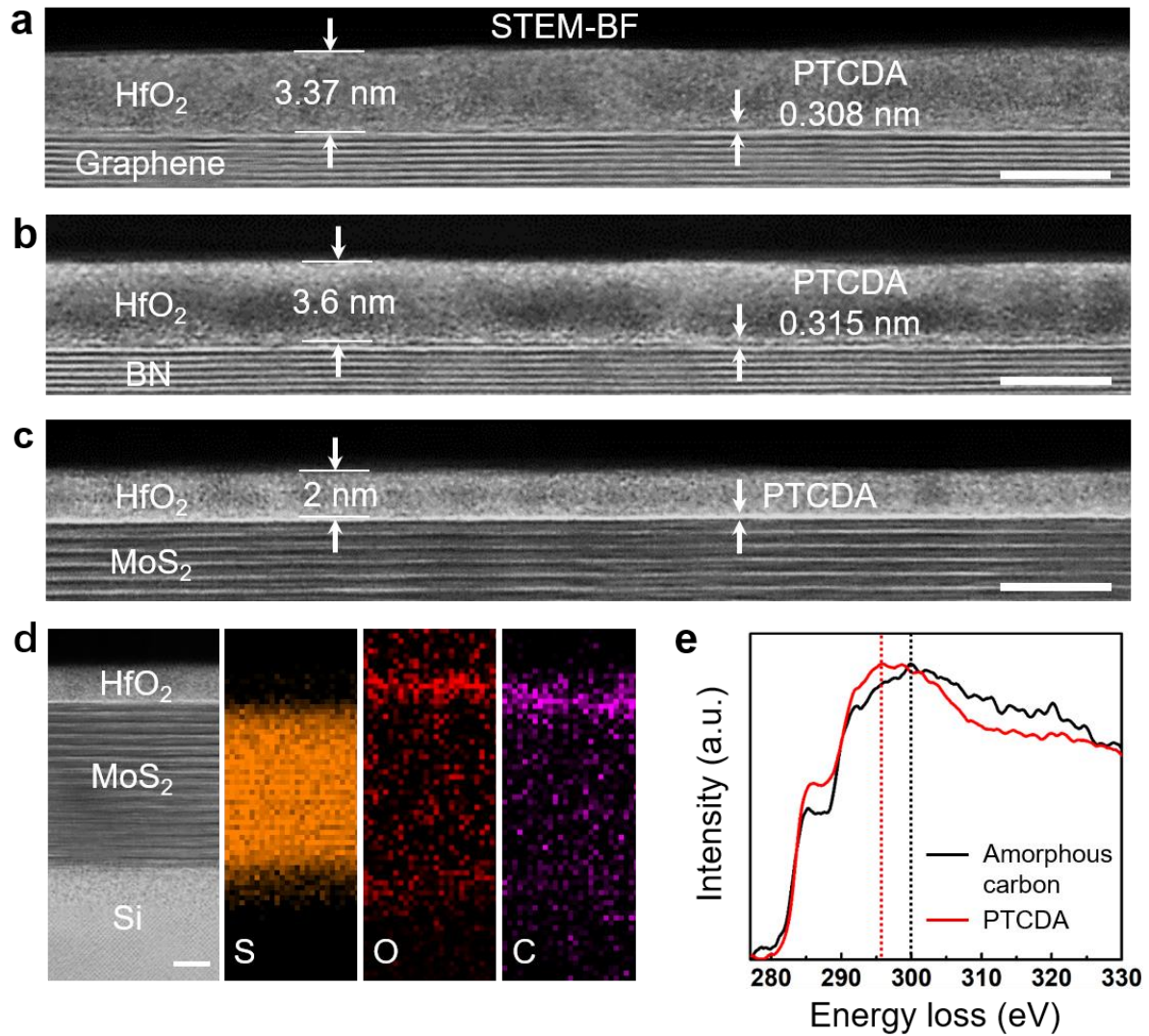


Figure 2. **STEM characterization of gate stacks.** **a-c.** Cross-sectional STEM Bright-field image of ML PTCDA/HfO₂ on graphene (**a**), MoS₂ (**b**) and h-BN (**c**), respectively. Scale bar are 5 nm. The thickness of HfO₂ and PTCDA layer is marked, respectively. **d.** STEM-EELS mapping. From left to right, STEM bright-field image and corresponding elemental mapping of S, O and C respectively. Scale bar is 2.5 nm **e.** EELS spectra of carbon *K*-edge signal from PTCDA at the HfO₂/MoS₂ interface (the high intensity area of C in **d**) and amorphous carbon from other positions.

Dielectric properties on graphene FETs

To study the dielectric properties, we fabricated double-gate graphene FET structure with 275 nm SiO₂/Si as the global backgate and ML PTCDA/HfO₂/Au as the top-gate stack (Fig. 3a

inset). Double-sweep I_D - V_{TG} transfer characteristics showed mobility $\mu \sim 3500 \text{ cm}^2/\text{Vs}$, no hysteresis and residual carrier density on the order of 10^{11} cm^{-2} (Fig. 3a, Supplementary Fig. S6), typical for graphene FET on SiO_2 ²⁹. The fabrication of top-gate did not introduce defects, doping or interface states as corroborated by the step-by-step electrical measurements (Supplementary Fig. S6). To accurately extract topgate capacitance (C_{TG}) and EOT, we used two independent methods, namely double-gate measurement on graphene FET (Fig. 2b, Supplementary Fig. S7) and capacitance measurement (C - V and C - f) (Supplementary Fig. S8). Capacitance measurement was performed on graphite (MoS_2)/ML PTCDA/ HfO_2 /Au capacitors on quartz substrate to eliminate parasitic capacitance. Theoretically, C_{TG} comprises of contributions from both PTCDA and HfO_2 :

$$\frac{1}{C_{TG}} = \frac{t_{PTCDA}}{\epsilon_0 \epsilon_{PTCDA}} + \frac{t_{ox}}{\epsilon_0 \epsilon_{ox}} \quad (1)$$

where t_{PTCDA} (t_{ox}) and ϵ_{PTCDA} (ϵ_{ox}) is physical thickness and dielectric constant of PTCDA (HfO_2), and ϵ_0 is vacuum dielectric constant. EOT is calculated as

$$EOT = \frac{3.45 \mu\text{F}/\text{cm}^2}{C_{TG}} \quad (2)$$

where $3.45 \mu\text{F}/\text{cm}^2$ is the gate capacitance for 1 nm SiO_2 . The effective dielectric constant of the whole stack (PTCDA+ HfO_2) is calculated as

$$\epsilon_{eff} = \frac{C_{TG}(t_{PTCDA}+t_{ox})}{\epsilon_0} \quad (3)$$

Fig. 3c summarizes the EOT and ϵ_{eff} as a function of t_{ox} measured from 30 graphene FETs, 35 MoS_2 FETs and 6 capacitors (4 graphene and 2 MoS_2). The four sets of data give nearly identical results, showing excellent reproducibility on different 2D materials. The EOT scales linearly with t_{ox} and intercepts the Y axis at 0.6 nm, which corresponds to the EOT of ML PTCDA. Both EOT and ϵ_{eff} are well described by theory (see the fittings in Fig. 3c) using $\epsilon_{PTCDA}=1.9$ and $\epsilon_{ox}=16.8$ consistent with literatures^{19, 30}. Remarkably, we fabricated several working devices with $t_{ox}=1.45 \text{ nm}$ and $EOT=1 \text{ nm}$ using only 7 cycles of ALD ($C_{TG}/C_{BG}=276$, Fig. 3b). Both t_{ox} and EOT are record-low on topgate 2D FETs (Table S1, S2). This further proves that the ML PTCDA layer is defect-free across the entire channel region. For comparison, ALD seeded by evaporated PTCDA on graphene/ SiC only achieved lowest $t_{ox}=10 \text{ nm}$ and $EOT=3.87 \text{ nm}$ without gate failure¹⁹.

Organic dielectrics generally suffer from low operating frequency³¹. However, the capacitance of PTCDA/ HfO_2 maintained nearly constant up to 1 MHz (Supplementary Fig. S8).

To test whether the gate dielectric functions at higher frequency, we fabricated ground-signal-ground graphene radio-frequency (RF) transistors on highly resistive Si substrate (Fig. 3e inset), with channel length of 500 nm, gate length (L_g) of 360 nm and $t_{ox}=6$ nm (EOT=2 nm). The device showed $\mu \sim 2000$ cm²/Vs and transconductance of 48 μ S/ μ m under $V_D=0.05$ V (Supplementary Fig. S9). Owing to the ultrathin EOT, the transconductance (scaled by V_D) was nearly one order of magnitude higher than similar device with $L_g=550$ nm and comparable to the self-aligned structure with $L_g=300$ nm^{32,33}. Fig. 3e plots the small-signal current gain $|h_{21}|$ extracted from the measured S parameters from 60 MHz to 20 GHz using an Agilent N5247A network analyzer. The $|h_{21}|$ showed a typical $1/f$ frequency dependence expected for an ideal FET, and the cut-off frequency (f_T) of 10.9 GHz was obtained from the linear fit. We further performed careful de-embedding using the exact pad layout as “open,” “short,” and “through” structures on the same chip³². The intrinsic f_T reached 60 GHz, which outperformed previously reported graphene RF transistors (under the same L_g) by more than 100%³³. We conclude that the PTCDA layer does not degrade the dielectric properties up to tens of GHz.

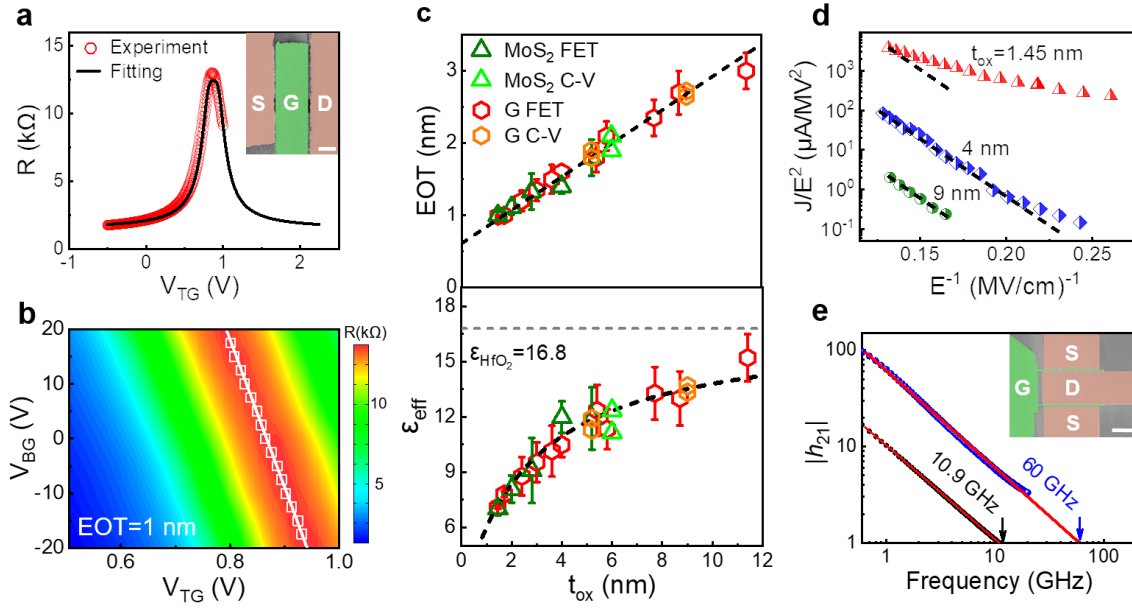


Figure 3. Dielectric properties on graphene FETs. **a.** Double-sweep resistance- V_{TG} characteristics of a topgate graphene FET with 7 cycles of ALD HfO₂ (symbols) and theoretical fitting (line). Inset shows false color SEM image of the device structure. Scale bar is 2 μ m. **b.** Resistance as a function of V_{TG} and V_{BG} of the same device in **a**. The Dirac points are shown by the white symbols, and linear fitting yields EOT=1 nm. **c.** EOT (top panel) and ϵ_{eff} (bottom panel) as a function of t_{ox} . Red (orange) hexagon and green (bright green) triangle

symbols represent results from graphene FET (capacitor) and MoS₂ FET (capacitor) measurements, respectively. Dashed lines are theoretical fittings. The bar graph shows the mean values (n = 30 for graphene FETs, n=35 for MoS₂ FETs), and error bars are the standard deviation. **d.** F-N plot of leakage current for t_{ox} =9 nm (green), 4 nm (blue), and 1.45 nm (red). The dashed lines are linear relationship as expected for F-N tunneling. **e.** Small-signal current gain $|h_{21}|$ measured from a graphene FET with channel length of 500 nm and L_g =360 nm before (black symbol) and after (blue symbol) de-embedding. Measurement conditions: V_D =1 V, V_{TG} =-0.4 V. Red lines are linear fittings to extract f_T . Inset shows false color SEM image of the device. Scale bar is 4 μ m.

As t_{ox} reduces, gate leakage from quantum mechanical tunneling becomes a major source of power consumption in integrated circuits. We investigated the tunneling mechanism for a wide range of t_{ox} . For t_{ox} =9 nm, the leakage current could be well described by Fowler-Nordheim (F-N) tunneling through a triangular potential barrier, $J \sim E_{ox}^2 \exp(-B/E_{ox})$, where E_{ox} is electric field in the oxide (see F-N plot in Fig. 3d). For t_{ox} =4 nm, J deviated from straight line in F-N plot at low field, suggesting that direct tunneling started to become significant. For t_{ox} =1.45 nm (EOT=1 nm), direct tunneling became dominant and led to exponential increase of leakage and complete deviation from F-N fitting. Nevertheless, the leakage current was reversible and dielectric did not breakdown until V_{TG} =3.27 V (Supplementary Fig. S10), suggesting excellent uniformity even down to such extreme thickness. We emphasize that the insertion of ML PTCDA significantly reduces the gate leakage and increases the breakdown field. Quantitative assessment and benchmark with other technologies will be discussed in the last section.

Low-power TMD CMOS

After characterizing the dielectric properties, we next integrated ML PTCDA/HfO₂ on TMDs for high on/off ratio CMOS. MoS₂ and WSe₂ were selected as representative channel materials for NMOS and PMOS, respectively. The device structure was similar to graphene FET (Fig. 4a), but with the backgate oxide changed to 30 nm Al₂O₃ to screen the Coulomb impurities³⁴. Fig. 4b and c present transfer and output characteristics of ML MoS₂ and WSe₂ FETs with t_{ox} =3 nm (EOT=1.3 nm, obtained from double-gate measurement). The NMOS

(PMOS) exhibits on/off ratio of 10^7 (10^6) and near-Boltzmann-limit SS of 60 (67) mV/dec. The SS is maintained for several orders of I_D for both sweeping directions (Supplementary Fig. S11b). The output characteristics are linear at low V_D , indicating Ohmic contacts. Importantly, I_D already shows saturation at $V_D=0.8$ V because of channel pinch-off enforced by small EOT. This allows us to reduce the operation voltage of TMD-based CMOS to state-of-the-art Si CMOS for the first time^{11, 15, 16, 30, 35}. The ultrathin EOT further allows us to realize a 2D CMOS inverter with gain of over 12 V/V at $V_{dd}=0.5$ V (Fig. 4c and Supplementary Fig. S12). Benefit from the low V_{dd} , the static and dynamic power consumption of the inverter is less than 0.6 nW and 0.8 nW, respectively, superior to any reported 2D inverters³⁶. Therefore, our dielectric integration technology truly enables the benefit of 2D channel in reducing the power consumption of integrated circuit. Like graphene FET, we also achieved the lowest EOT=1 nm on MoS₂ NOMS with SS = 61 mV/dec (Supplementary Fig. S11). To further evaluate the process reproducibility, we measured 20 MoS₂ (1-3 layer) NMOS with $t_{ox}=3$ nm. The average two-terminal mobility, SS and EOT was 34 cm²/Vs, 66 mV/dec and 1.35 nm, respectively (Fig. 3e, f). Both SS and EOT showed narrow Gaussian distribution with less than 15% variation (measured by the full-width-of-half-maximum from the Gaussian fit). On the other hand, control devices with 3 nm neat HfO₂ topgate dielectric shows serious leakage due to the non-uniform nucleation.

The 60mV/dec switching, hysteresis-free transfer characteristics (Supplementary Fig. S13) and small frequency dispersion of $C-V$ curves (Supplementary Fig. S8) consistently suggest very low D_{it} . To quantitatively analyze the interface properties, we performed modeling of I_D - V_{TG} characteristics by considering the MoS₂ channel carrier statistics through quantum capacitance and transport through Drude model³⁷. To avoid the underestimation of D_{it} , we adopted a conservative approach and analyzed ML MoS₂ FETs with relatively large EOT=2.1 nm. Fig. 3g shows the extracted D_{it} distribution. At the mid-gap region corresponding to the small-current subthreshold region with constant SS, D_{it} is as low as $\sim 8 \times 10^{11}$ cm⁻²eV⁻¹ and gradually increases to the range of 10^{12} cm⁻²eV⁻¹ toward the conduction band edge. Compared with previous metal-buffered ALD MoS₂ FETs³⁷ and other top-gate MoS₂ FETs^{15, 30, 38-41}, our device shows the lowest D_{it} at the mid-gap region, which indicates that the ideal SS is not only due to the ultrathin EOT but also due to the improved interface properties. The origin for this improvement is attributed to the non-invasive and atomically flat nature of the PTCDA buffer

layer, low strain due to van der Waals separation as well as indirect ALD deposition. The dense and pinhole-free oxide also well encapsulates the MoS₂ channel to give excellent long-term stability of the devices (Supplementary Fig. S14).

Moving forward to integration, it is important to demonstrate uniform dielectric deposition on large-area films. To this end, we deposited ML PTCDA/HfO₂ on centimeter-scale CVD MoS₂ transferred off sapphire substrate. Similar to exfoliated samples, conformal deposition was realized despite unavoidable PMMA residues from the transfer process (Supplementary Fig. S15). We next fabricated topgate transistor arrays using standard top-down lithography and etching processes (Fig. 4h-i, see Supplementary Fig. S16 for the process flow). Even though the process involved multiple steps of lithography, we were still able to achieve device yield of 90% (without gate failure). The transfer characteristics of 27 devices show small variations in threshold voltage and SS (Fig. 4i). The average SS of 160 mV/dec is much larger than exfoliated MoS₂ devices, which is attributed to thicker oxide ($t_{ox}=6$ nm) and additional interface states associated with CVD samples. We also developed new transfer technology of CVD TMDs using PTCDA/oxide stack instead of widely used polymers as support layer (see Method and Supplementary Fig. 17). Centimeter-scale continuous CVD MoS₂ film on sapphire could be transferred to target substrate with high integrity, extremely clean interface and small roughness. Compared to conventional approaches, our method can avoid any polymer and solvent contaminations on TMDs surface and form high-quality dielectric interface on large-area films. With further process optimization, it can provide a new path for TMD-based large-scale integrated circuits.

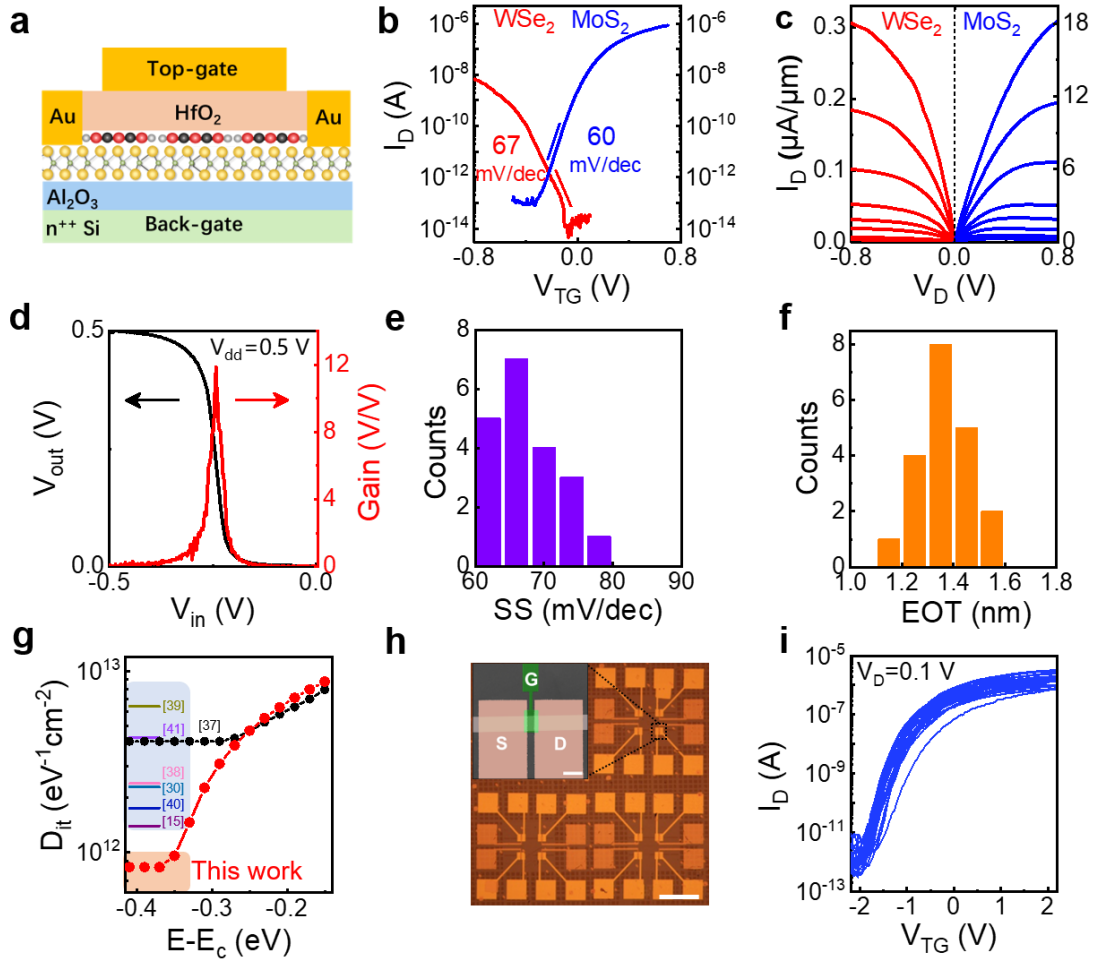


Figure 4. **Low-power TMD CMOS.** **a.** Schematic of the device structure. **b.** Transfer characteristics of a ML MoS₂ NMOS (blue) and WSe₂ PMOS (red) with $t_{ox}=3$ nm and EOT=1.3 nm. The SS values are marked on the plot. Measured under $V_D=0.5$ V for both devices, and $V_{BG}=0$ V (-8 V) for MoS₂ (WSe₂). **c.** Output characteristics of the same devices in **b.** For the MoS₂ device, from top to bottom, V_{TG} from 0.5 V to -0.3 V with 0.1 V step, $V_{BG}=15$ V to turn on the ungated region. For the WSe₂ device, from top to bottom, V_{TG} from -2 V to -1.2 V with 0.1 V step, $V_{BG}=-15$ V to turn on the ungated region. The WSe₂ device shows much lower on-state current density than the MoS₂ device due to the crystal quality and contact resistance. **d.** Measured output voltage and gain as a function of input voltage of a CMOS inverter under $V_{dd}=0.5$ V. **e. f.** Statistical distribution of SS (**e**) and EOT (**f**) measured from 20 MoS₂ FETs with $t_{ox}=3$ nm. **g.** D_{it} distribution as a function of energy below the conduction band from a typical MoS₂ FET with EOT=2.1 nm, in comparison with mid-gap D_{it} values from literatures^{15, 30, 37-41}. **h.** Optical micrograph of MoS₂ FET arrays fabricated on CVD samples. Scale bar is

150 μm . Inset shows the false color SEM image of a CVD MoS₂ device. We adopted overlap structure between topgate and source/drain to minimize the ungated region⁴². Scale bar is 7 μm .

i. Transfer characteristics of 27 CVD MoS₂ FETs.

Short-channel MoS₂ FET

For Si CMOS, the industry has adopted tri-gate structure since 22 nm node because of the otherwise prohibitive SCE in planar devices⁴³. On the other hand, the combination of ultrathin EOT and 2D channel should in principle minimize SCE⁵. To prove this point, we designed and fabricated short-channel ($L_g \sim 20$ nm, limited by our lithographic resolution) MoS₂ FETs with graphene backgate and ML PTCDA/HfO₂ as gate dielectric (Fig. 5a, b, see Supplementary Fig. S18 for process flow). The MoS₂ was dry transferred onto the backgate stack⁴⁴. This structure can fully exploit the combination of ultrathin dielectric grown on 2D materials (in this case graphene) and ultra-scaled channel without complicated topgate alignment. Fig. 5c and d plot the transfer and output characteristics of a typical device with $L_g = 20$ nm and EOT = 2 nm. The device shows on/off ratio in excess of 10^7 and steep SS = 73 mV/dec, suggesting that the structure is indeed immune to SCE. The SS is lower than most reported MoS₂ FETs with similar channel length (Table S2) and is close to 69 mV/dec for 22 nm node Si tri-gate transistors⁴³. We note that the current density of our short-channel devices is limited by contact resistance, which will be optimized in future works.

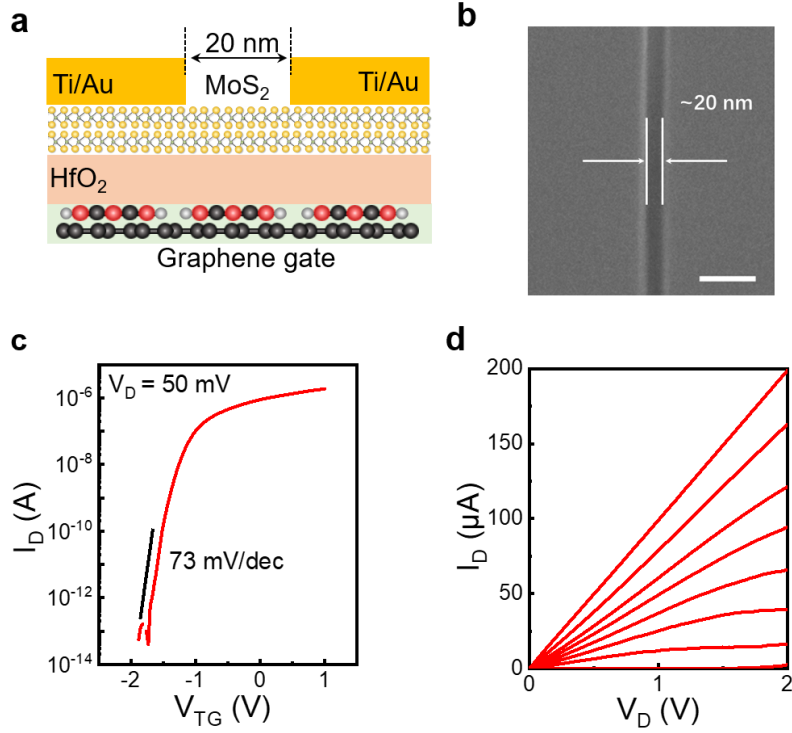


Figure 5. **Short-channel MoS₂ FETs.** **a.** Schematic of the device structure. **b.** SEM image of a device with $L_g=20$ nm. Scale bar is 80 nm. **c.** Transfer characteristics of the device shown in **b**, measured under $V_D=50$ mV. **d.** Output characteristics of the same devices in **c** under $V_{BG}=0$ V. From top to bottom, V_{TG} from -2 V to 2 V with 0.5 V step.

Benchmark with other technologies

In order to critically assess the potential for applications, it is important to benchmark with mature Si technology and other approaches on 2D materials. The breakdown characteristics (Fig. 6a) and gate leakage (Fig. 6b) are most important factors for reliability and power consumption. Fig. 6a plots the breakdown voltage (V_{bd}) and field ($E_{bd} = \frac{V_{bd}}{t_{PTCDA} + t_{ox}}$) of topgate graphene FETs (Supplementary Fig. S10) as a function of EOT. We find that V_{bd} increases linearly with EOT in the whole range, and a linear fitting yields a constant maximum carrier density $n_{max} = \frac{C_{TG} V_{bd}}{e} = \frac{\epsilon_{SiO_2} \epsilon_0}{e} \frac{V_{bd}}{EOT} = 6.5 \times 10^{13} \text{ cm}^{-2}$. This is the highest carrier density achieved in 2D materials using oxide^{11, 16, 19, 30, 45}, even close to that of ionic liquid gating⁴⁶. On the other hand, E_{bd} shows the opposite trend of decreasing with EOT (and ϵ_{eff}), which is in

accordance with $E_{bd} \sim \epsilon^{-1/2}$ for high- κ materials⁴⁷ (see the blue dashed line in Fig. 6a for theoretical fitting). The E_{bd} is within the theoretical limits predicated for HfO₂ (4-8 MV/cm)⁴⁷ at large EOT but rapidly increases to 16.5 MV/cm at 1 nm EOT. This indicates that the ML PTCDA actually controls the breakdown at small EOT, which again proves its excellent quality as buffer layer. Under the same EOT, our V_{bd} is significantly higher than most literature results on 2D materials using metal and organic buffer layer^{11, 16, 19, 30, 45}. Compared with the best result of 5 nm Hf/HfO₂ on graphene (EOT=1.38 nm) reported by Samsung⁴⁸, our V_{bd} is similar but E_{bd} is increased by more than 25%.

Fig. 6b compares the gate leakage current of topgate graphene and MoS₂ FETs with available data on Si CMOS^{2, 49} and 2D materials^{11, 14, 16, 19, 30, 45, 48}, under the same $V_{TG}=1$ V. Surprisingly, our data points almost overlap with HfO₂/Si deposited by advanced industrial tools⁴⁹, and are orders of magnitude lower than SiO₂/Si and most 2D data. Even at 1 nm EOT, the leakage current satisfies the low-power requirement for CMOS (1.5×10^{-2} A/cm²)⁴⁹. Although BN is considered as an ideal dielectric for 2D materials, the leakage current of graphene/BN/graphene structure at EOT=1 nm is over 5 orders of magnitude higher than our results⁴⁹. Therefore, BN is not suitable for low-power 2D transistors. We note that although the PTCDA layer decreases ϵ_{eff} at small EOT, the leakage current does not deviate from standalone HfO₂ on Si. This is probably due to the 0.3 nm-wide van der Waals gap between PTCDA and 2D materials, which effectively suppresses the tunnel current.

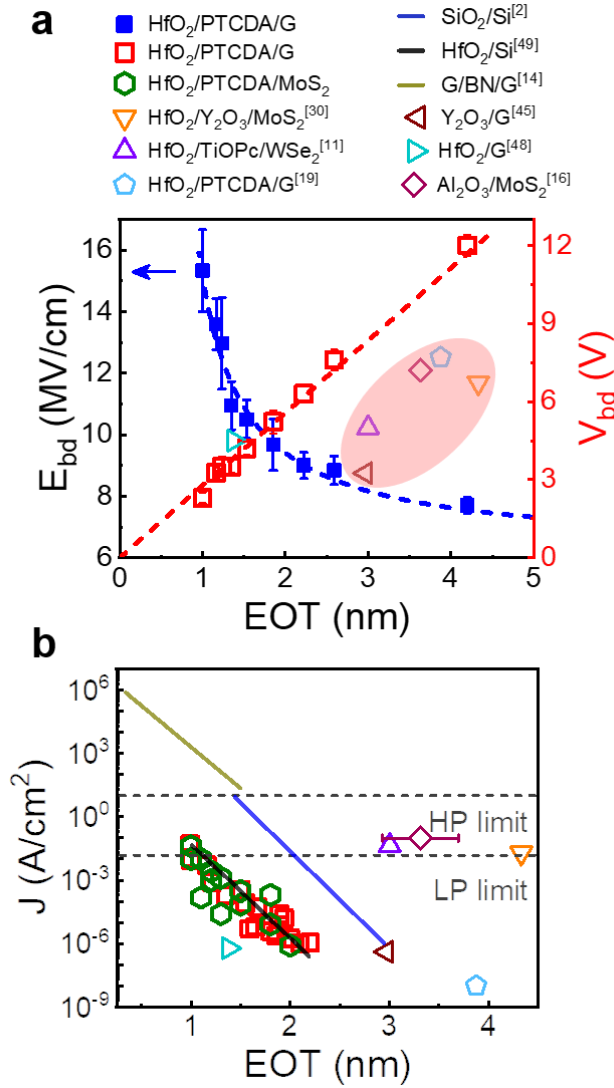


Figure 6. **Benchmark of breakdown and leakage characteristics with other technologies.**

a. E_{bd} (closed symbols, left axis) and V_{bd} (open symbols, right axis) as a function of EOT measured from topgate graphene FETs, in comparison with 2D data from literature^{11, 16, 19, 30, 45, 48}. The dashed red line is linear fitting of V_{bd} which gives maximum carrier density of $6.5 \times 10^{13} \text{ cm}^{-2}$. The blue dashed line is the theoretical fitting by $E_{bd} \sim \epsilon_{eff}^{-1/2}$, where the $\epsilon_{eff} - \text{EOT}$ relationship is obtained from Fig. 3c. The bar graph shows the mean values ($n = 30$), and error bars are the standard deviation. **b.** Leakage current (under $V_{TG} = 1 \text{ V}$) as a function of EOT measured from topgate graphene (red symbols) and MoS₂ (green symbols) FETs, in comparison with Si and 2D data from literature^{11, 16, 19, 30, 45, 48}. The black, blue and gold solid lines are leakage current of HfO₂/Si⁴⁹, SiO₂/Si² and graphene/BN/graphene¹⁴. The two

horizontal dashed lines are the ITRS limit for high-performance and low-power logic applications².

Conclusion and outlook

In conclusion, we achieved record-low EOT=1 nm on graphene and TMDs using self-limited ML molecular crystal as buffer layer. The gate dielectric shows pristine interface quality, low leakage current and high breakdown field simultaneously. For the first time, the leakage current is reliably reduced to the level of Si CMOS and comply with the low-power requirement down to 1 nm EOT. The combined EOT and interface integrity lead to ideal 60 mV/dec switching, low V_{dd} =0.8 V, and reduced SCE in TMD transistors. Our process has little variations on different 2D materials, and is applicable to large-area CVD films. Although we exclusively use HfO₂ in this work, our method is generally applicable to any oxides that can be deposited by ALD (see Fig. S19 for additional data on Al₂O₃). With higher ϵ_{ox} oxides such as ZrO₂ (ϵ_{ox} =35)⁵⁰, it is possible to achieve EOT=0.77 nm at t_{ox} =1.5 nm. Further reduction of EOT would require the substitution of low- κ organic seeding layer (while maintaining the same uniformity), which is very challenging. High-performance integrated circuits will require more efforts toward cleaner CVD growth, transfer and fabrication processes that minimize surface impurities¹⁸.

Data availability

The data that support the plots within this paper and other findings of this study are available from the corresponding author upon reasonable request.

References:

1. Theis, T.N. & Wong, H.S.P. The End of Moore's Law: A New Beginning for Information Technology. *Comput. Sci. Eng.* **19**, 41-50 (2017).
2. Natarajan, S. et al. A 14nm Logic Technology Featuring 2nd-Generation FinFET Interconnects, Self-Aligned Double Patterning and a 0.0588 μm^2 SRAM cell size. *Inter. Electron Dev. Meet. Tech.*

- Digest 3.7.1-3.7.3 (2014).*
3. Robertson, J. High dielectric constant oxides. *Eur. Phys. J-Appl. Phys.* **28**, 265-291 (2004).
 4. Chhowalla, M.D.J.A. Two-dimensional semiconductors for transistors. *Nat. Rev. Mater.* **11**, 16052 (2016).
 5. Fiori, G. et al. Electronics based on two-dimensional materials. *Nat. Nanotechnol.* **9**, 768-779 (2014).
 6. Desai, S.B. et al. MoS₂ transistors with 1-nanometer gate lengths. *Science* **354**, 99-102 (2016).
 7. Radisavljevic, B., Radenovic, A., Brivio, J., Giacometti, V. & Kis, A. Single-layer MoS₂ transistors. *Nat. Nanotechnol.* **6**, 147-150 (2011).
 8. Kim, H.G. & Lee, H. Atomic Layer Deposition on 2D Materials. *Chem. Mater.* **29**, 3809-3826 (2017).
 9. Zhu, Y. et al. Monolayer Molybdenum Disulfide Transistors with Single-Atom-Thick Gates. *Nano Lett.* **18**, 3807-3813 (2018).
 10. Wang, X., Tabakman, S.M. & Dai, H. Atomic Layer Deposition of Metal Oxides on Pristine and Functionalized Graphene. *J. Am. Chem. Soc.* **130**, 8152-8153 (2008).
 11. Park, J.H. et al. Atomic Layer Deposition of Al₂O₃ on WSe₂ Functionalized by Titanyl Phthalocyanine. *ACS Nano* **10**, 6888-6896 (2016).
 12. Alaboson, J.M.P. et al. Seeding Atomic Layer Deposition of High- κ Dielectrics on Epitaxial Graphene with Organic Self-Assembled Monolayers. *ACS Nano* **5**, 5223-5232 (2011).
 13. Johns, J.E., Karmel, H.J., Alaboson, J.M.P. & Hersam, M.C. Probing the Structure and Chemistry of Perylenetetracarboxylic Dianhydride on Graphene Before and After Atomic Layer Deposition of Alumina. *J. Phys. Chem. Lett.* **3**, 1974-1979 (2012).
 14. Britnell, L. et al. Electron Tunneling through Ultrathin Boron Nitride Crystalline Barriers. *Nano Lett.* **12**, 1707-1710 (2012).
 15. Wang, J. et al. Integration of High-k Oxide on MoS₂ by Using Ozone Pretreatment for High-Performance MoS₂ Top-Gated Transistor with Thickness-Dependent Carrier Scattering

- Investigation. *Small* **11**, 5932-5938 (2015).
16. Wang, X. et al. Improved integration of ultra-thin high-k dielectrics in few-layer MoS₂ FET by remote forming gas plasma pretreatment. *Appl. Phys. Lett.* **110**, 53110 (2017).
 17. Xiao, M., Qiu, C., Zhang, Z. & Peng, L. Atomic-Layer-Deposition Growth of an Ultrathin HfO₂ Film on Graphene. *ACS Appl. Mater. Inter.* **9**, 34050-34056 (2017).
 18. Liu, Y. et al. Approaching the Schottky - Mott limit in van der Waals metal - semiconductor junctions. *Nature* **557**, 696-700 (2018).
 19. Sangwan, V.K. et al. Quantitatively Enhanced Reliability and Uniformity of High- κ Dielectrics on Graphene Enabled by Self-Assembled Seeding Layers. *Nano Lett.* **13**, 1162-1167 (2013).
 20. Dean, C.R. et al. Boron nitride substrates for high-quality graphene electronics. *Nat. Nanotechnol.* **5**, 722-726 (2010).
 21. Yang, L., et al. 10 nm nominal channel length MoS₂ FETs with EOT 2.5 nm and 0.52 mA/ μ m drain current. *73rd Annual Device Research Conference. IEEE*, 237-238(2015).
 22. Liao, L. et al. Top-Gated Graphene Nanoribbon Transistors with Ultrathin High- κ Dielectrics. *Nano Lett.* **10**, 1917-1921 (2010).
 23. Liao, L. et al. Sub-100 nm Channel Length Graphene Transistors. *Nano Lett.* **10**, 3952-3956 (2010).
 24. Cheng, R. et al. Few-layer molybdenum disulfide transistors and circuits for high-speed flexible electronics. *Nat. Commun.* **5**, 5143 (2014).
 25. Wu, B. et al. Precise, Self-Limited Epitaxy of Ultrathin Organic Semiconductors and Heterojunctions Tailored by van der Waals Interactions. *Nano Lett.* **16**, 3754-3759 (2016).
 26. Hersam, M.C. & Wang, Q.H. Room-temperature molecular-resolution characterization of self-assembled organic monolayers on epitaxial graphene. *Nat. Chem.* **1**, 206-211 (2009).
 27. Zhao, Y., Wu, Q., Chen, Q. & Wang, J. Molecular Self-Assembly on Two-Dimensional Atomic Crystals: Insights from Molecular Dynamics Simulations. *J. Phys. Chem. Lett.* **6**, 4518-4524 (2015).
 28. Martin, J.M., Vacher, B., Ponsonnet, L. & Dupuis, V. Chemical bond mapping of carbon by image-

- spectrum EELS in the second derivative mode. *Ultramicroscopy* **65**, 229-238 (1996).
29. Wang, X., Xu, J., Wang, C., Du, J. & Xie, W. High-Performance Graphene Devices on SiO₂/Si Substrate Modified by Highly Ordered Self-Assembled Monolayers. *Adv. Mater.* **23**, 2464-2468 (2011).
 30. Zou, X. et al. Interface Engineering for High-Performance Top-Gated MoS₂ Field-Effect Transistors. *Adv. Mater.* **26**, 6255-6261 (2014).
 31. Wang, B. et al. High-κ Gate Dielectrics for Emerging Flexible and Stretchable Electronics. *Chem. Rev.* **118**, 5690-5754 (2018).
 32. Cheng, R. et al. High-frequency self-aligned graphene transistors with transferred gate stacks. *Proc. Natl Acad. Sci. USA* **109**, 11588-11592 (2012).
 33. Wu, Y. et al. High-frequency, scaled graphene transistors on diamond-like carbon. *Nature* **472**, 74-78 (2011).
 34. Yu, Z. et al. Realization of Room-Temperature Phonon-Limited Carrier Transport in Monolayer MoS₂ by Dielectric and Carrier Screening. *Adv. Mater.* **28**, 547-552 (2016).
 35. International Technology Roadmap for Semiconductors. www.itrs.net/2013-itrs.html (Semiconductor Industry Association, 2013).
 36. Pu, J. et al. Highly Flexible and High-Performance Complementary Inverters of Large-Area Transition Metal Dichalcogenide Monolayers. *Adv. Mater.* **28**, 4111-4119 (2016).
 37. Fang, N. & Nagashio, K. Band tail interface states and quantum capacitance in a monolayer molybdenum disulfide field-effect-transistor. *J. Phys. D* **51**, 65110 (2018).
 38. Liu, H. & Ye, P.D. MoS₂ Dual-Gate MOSFET With Atomic-Layer-Deposited Al₂O₃ as Top-Gate Dielectric. *IEEE Electr. Dev. Lett.* **33**, 546-548 (2012).
 39. Salvatore, G.A. et al. Fabrication and Transfer of Flexible Few-Layers MoS₂ Thin Film Transistors to Any Arbitrary Substrate. *ACS Nano* **7**, 8809-8815 (2013).
 40. Ninomiya, N. et al. Fabrication of high-k/metal-gate MoS₂ field-effect transistor by device isolation process utilizing Ar- plasma etching. *J. Appl. Phys. Jpn* **54**, 046502 (2015).

41. Choi, K. et al. Trap density probing on top-gate MoS₂ nanosheet field-effect transistors by photo-excited charge collection spectroscopy. *Nanoscale* **7**, 5617 (2015).
42. Zhong, D. et al. Gigahertz integrated circuits based on carbon nanotube films. *Nat. Electron.* **1**, 40-45 (2018).
43. Auth, C. et al. A 22nm high performance and low-power CMOS technology featuring fully-depleted tri-gate transistors, self-aligned contacts and high density MIM capacitors. *Symp. VLSI Tech.* 131-132 (2012).
44. Wang, L. et al. One-dimensional electrical contact to a two-dimensional material. *Science* **342**, 614-617 (2013).
45. Takahashi, N. & Nagashio, K. Buffer layer engineering on graphene via various oxidation methods for atomic layer deposition. *Appl. Phys. Express* **9**, 125101 (2016).
46. Xia, Jilin, et al. Measurement of the quantum capacitance of graphene. *Nat. Nanotechnol.* **4**, 505-509 (2009).
47. McPherson, J., Kim, J., Shanware, A. & Mogul, H. Thermochemical description of dielectric breakdown in high dielectric constant materials. *Appl. Phys. Lett.* **82**, 2121-2123 (2003).
48. Jeong, S. et al. Thickness scaling of atomic-layer-deposited HfO₂ films and their application to wafer-scale graphene tunnelling transistors. *Sci. Rep.* **6** 20907 (2016).
49. Gusev, E.P. et al. Ultrathin high- κ gate stacks for advanced CMOS devices. *Inter. Electron Dev. Meet. Tech. Digest* 20.1.1-20.1.4 (2001).
50. Johannes Muller. et al. Ferroelectricity in simple binary ZrO₂ and HfO₂. *Nano Lett.* **12**, 4318-4223(2012).

Acknowledgements. This work is supported by National Natural Science Foundation of China 61734003, 61521001, 51861145202, 61861166001, 11874199, 21872100; National Key Basic Research Program of China 2015CB921600, 2015CB654901; Natural Science Foundation of Jiangsu Province under BK20170005; Singapore MOE Grant R143-000-A43-114; the Program A for Outstanding Ph.D. candidate of Nanjing University 201801A013; Postgraduate Research

& Practice Innovation Program of Jiangsu Province KYCX18_0045; Strategic Priority Research Program of Chinese Academy of Sciences XDB 30000000; a Grant-in-Aid for JSPS Research Fellows from the JSPS KAKENHI; Key Laboratory of Advanced Photonic and Electronic Materials, Collaborative Innovation Center of Solid-State Lighting and Energy-Saving Electronics, and the Fundamental Research Funds for the Central Universities, China.

Author Contributions. X.Wang conceived and supervised the project. W.L., J. Zhou, Z.Y., N.D., X.Wu., H.Z., D.H. Y.S. and X.D. contributed to sample preparation, characterization, device fabrication, measurements and data analysis. S.C. and P.W. performed TEM and data analysis. J.Zhang. and W.C. performed STM and data analysis. N.F. and K.N. performed D_{it} analysis. T.L. and Z.W. performed CVD sample growth and transfer. Y.W. and T.C. contributed to RF transistor fabrication, measurements and data analysis. X.X. and H.M. performed molecular dynamics simulations. K.Y. and L.P. performed water contact angle measurement. W.L., Z.Y., P.W. and X.Wang wrote the manuscript with input from other authors. All authors contributed to discussions.

Competing financial interests

The authors declare no competing financial interests.

Methods

Growth of ML PTCDA on 2D materials. The growth of ML PTCDA was carried out in a home-built single-zone vacuum tube furnace. A crucible containing PTCDA powder (95%, Alfa Aesar) was placed in the center of the heating zone. Exfoliated or CVD 2D materials were placed downstream several centimeters away from the center. A turbo molecular pump was used to evacuate the quartz tube to $\sim 4 \times 10^{-5}$ Pa. Then, the source powder was heated to a target temperature of 250-280 °C (depending on the 2D materials) for ~ 20 minutes before cooling down naturally.

ALD of HfO₂. ALD was carried out at 150°C and base pressure of ~ 5 Pa using Tetrakis(dimethylamido) hafnium and H₂O as precursors. We used 30 sccm N₂ as carrier gas. The pulse/purge time for Hf and H₂O precursors were 250 ms/60 s and 100 ms/60 s, respectively.

STM Characterization. STM measurements were carried out at 77 K in an ultrahigh vacuum

chamber (Unisoku LT-STM) with base pressure better than 1.0×10^{-10} mbar. The STM imaging were performed using constant current mode with a commercial Pt-Ir tip. All the bias voltages were applied to the sample. For better conductivity, we used monolayer CVD graphene on Cu as the substrate, which was thoroughly degassed at 500 °C in the UHV chamber before in-situ PTCDA deposition. PTCDA are thermally evaporated from Knudsen cells at 280 °C onto the clean graphene/Cu substrate kept at 105 °C. Prior to deposition, the molecular source was purified by gradient vacuum sublimation.

Calculation of binding energy. Molecular mechanics method was applied to calculate the binding energies of PTCDA molecules on 2D materials via Forcite module in Materials Studio 7.0 package (Accelrys) by $E_{BE} = E_{PTCDA} + E_{sub} - E_{PTCDA@sub}$. Here $E_{PTCDA@sub}$, E_{PTCDA} and E_{sub} are total energy of PTCDA molecule adsorbed on the substrate, isolated PTCDA and substrate, respectively. In this case, universal force field (UFF) was used.

Cross-sectional TEM sample fabrication and STEM characterization. TEM samples of Au/HfO₂/ML PTCDA/2D materials structure were fabricated using FEI Helios 600i dual-beam focused ion beam (FIB) system. Pt protection layer was first deposited on the top surface of the devices, followed by etching surrounding area to form the sample lamella using 30 kV accelerating voltage and 21 nA gallium ion beam. The lamella was then lift out from silicon substrate and directly transferred to a TEM half grid inside the FIB chamber. We further thinned the observation area down to less than 100 nm with tens to hundreds pA gallium beam current. Finally, 5 kV accelerating voltage with 0.12 nA and 2 kV accelerating voltage with a smaller current of 68 pA was subsequently used for fine polishing to remove the damage layers present on both sides of the prepared TEM samples.

STEM characterization was acquired on a FEI Titan G2 60-300 aberration corrected S/TEM microscope with the accelerating voltage of 300kV. Bright-field (BF) imaging mode was used for the device observation. Unlike Z-contrast image, a BF image shows phase contrast, so it is much more applicable to distinguish light atoms from heavy ones. Gatan dual-EELS system was used for STEM-EELS data acquisition. For EELS mapping, the acquisition time per pixel was 0.1 s to reduce beam damage. The total acquisition energy range was 60 to 572

eV, including carbon *K*-edge, sulfur *L*-edge and oxygen *K*-edge. By integrating the signal of corresponding energy loss edges from STEM-EELS images, the distribution of those elements can be mapped.

CVD MoS₂ growth and transfer. Centimeter-size MoS₂ films were grown by the way of low-pressure CVD on sapphire substrate using MoO₃ powder and S powder as sources, under 950 °C. To transfer CVD MoS₂ film off sapphire using ML PTCDA/HfO₂ stack, we first grew ML PTCDA and HfO₂ on freshly grown CVD samples using preceding method. PMMA was spin coated at a speed of 2000 R.P.M. for 1 min and then cured at 70 °C for 10 min, followed by lamination of thermal release tape. Next, the sample was immersed in deionized water and the whole stack was spontaneously delaminated from sapphire and transferred onto a target substrate. Finally, the thermal release tape was removed by baking at 150 °C, and PMMA was removed by soaking in acetone.

Topgate transistor fabrication. All the topgate devices shared similar fabrication procedures. First, source/drain electrodes were patterned. Then, ML PTCDA and HfO₂ were deposited onto the channel area using preceding method. Finally, gate electrode was align patterned between source and drain. For exfoliated graphene/TMD transistors, 80 nm Au was used as source/drain/gate electrodes. For graphene RF transistors, 5 nm Ti/70 nm Pd was used as source/drain/gate electrodes to enhance adhesion and reduce parasitic resistance. For CVD MoS₂ transistors, 10 nm Ti/50 nm Au (5 nm Ti/15 nm Au) was used as source/drain (gate) electrodes.

Short-channel MoS₂ transistor fabrication. Few-layer graphene was mechanically exfoliated onto 275 nm SiO₂/Si substrate. Then, Au was contacted to the graphene as gate electrode. ML PTCDA and 6 nm HfO₂ was deposited onto graphene as gate dielectric using preceding methods. MoS₂ was align transferred onto HfO₂/ML PTCDA/graphene stack using pole-propylene carbonate film. Source and drain electrodes were patterned by EBL. We deposited 1 nm Ti/10 nm Pd metal electrodes to minimize the fringing field and SCE.

Electrical measurements. Electrical measurements of graphene and TMD devices were carried out by an Agilent B1500 semiconductor parameter analyzer in a close-cycle cryogenic probe station with base pressure $\sim 10^{-6}$ Torr. *C-f* measurements were performed by Agilent

E4980 Precision LCR Meter. The on-chip microwave measurements of graphene RF transistors were carried out by using Agilent N5247A network analyzer under ambient environment.

Supplementary Information

Table of contents:

Supplementary Figure 1 | AFM characterization

Supplementary Figure 2 | Cross-polarized optical microscopy

Supplementary Figure 3 | Water contact angle measurement

Supplementary Figure 4 | Raman characterization

Supplementary Figure 5 | Cross-sectional STEM characterization

Supplementary Figure 6 | Step-by-step electrical measurements of topgate FET

Supplementary Figure 7 | Double-gate measurement to extract C_{TG}

Supplementary Figure 8 | Capacitance-frequency ($C-f$) measurement and capacitance-voltage ($C-V$) measurement to extract C_{TG}

Supplementary Figure 9 | DC performance of RF graphene transistor

Supplementary Figure 10 | Breakdown characteristics of ML PTCDA/HfO₂

Supplementary Figure 11 | Topgate MoS₂ EFT with 1 nm EOT

Supplementary Figure 12 | Ultra-low power CMOS inverter

Supplementary Figure 13 | Hysteresis of topgate MoS₂ FET

Supplementary Figure 14 | Long-term stability

Supplementary Figure 15 | AFM characterization of CVD MoS₂ film

Supplementary Figure 16 | Fabrication process of topgate FET array on CVD MoS₂

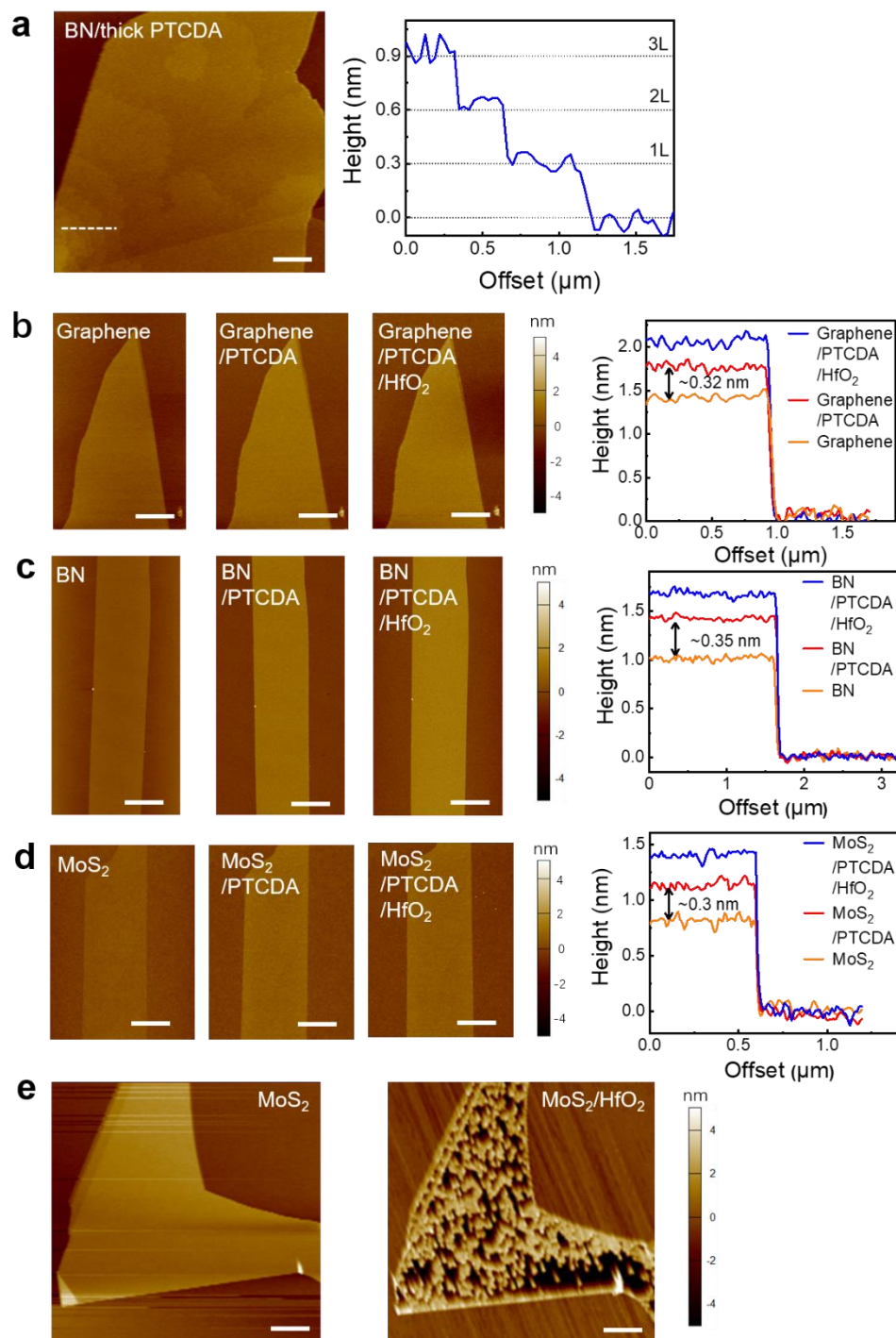
Supplementary Figure 17 | Transfer of CVD MoS₂ using ML PTCDA/HfO₂ stack as support layer

Supplementary Figure 18 | Fabrication process of short-channel MoS₂ FET

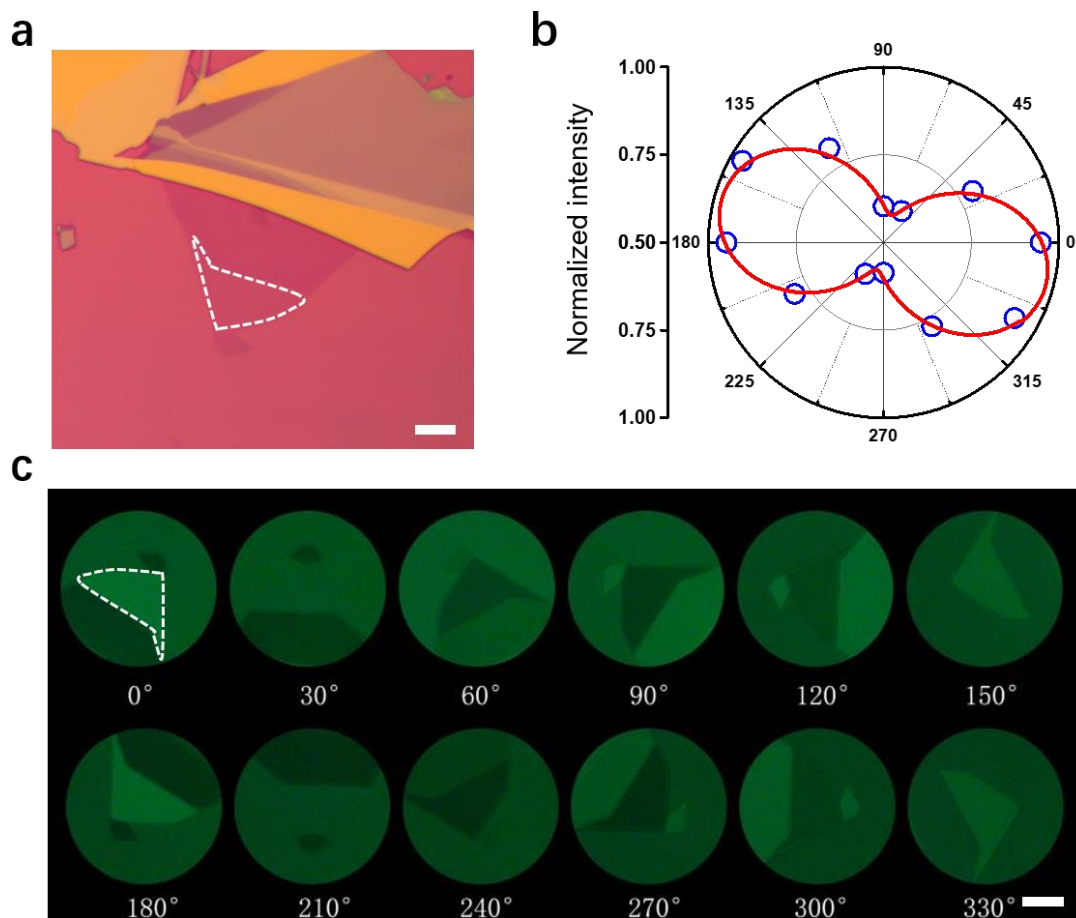
Supplementary Figure 19 | Topgate FET with Al₂O₃ as dielectric

Supplementary Table 1 | Comparison between the ML PTCDA assisted, ALD grown HfO₂ film and that grown by other methods on graphene

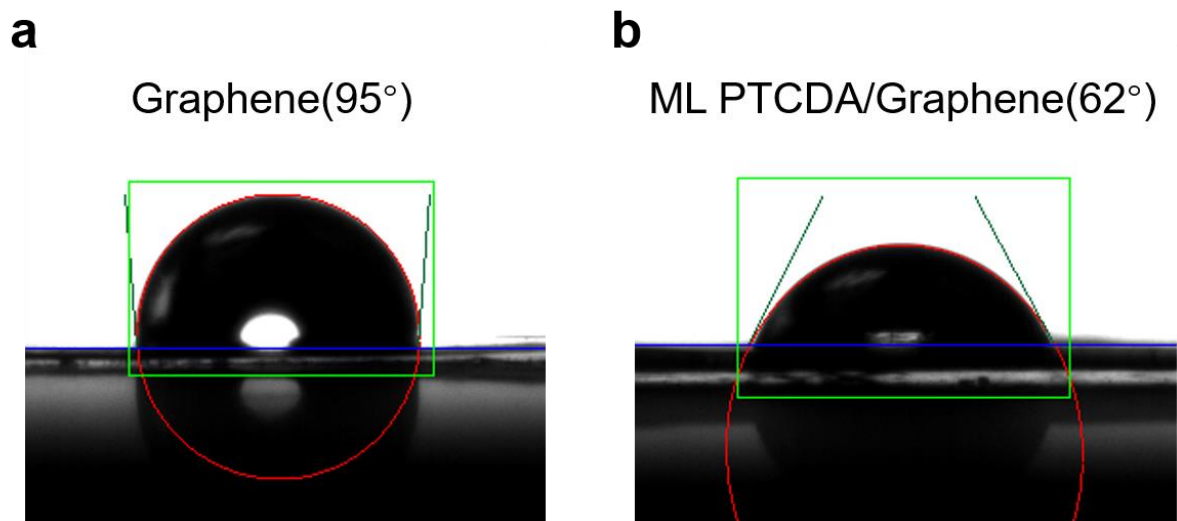
Supplementary Table 2 | Comparison between the ML PTCDA assisted, ALD grown HfO₂ film and that grown by other methods on TMDs



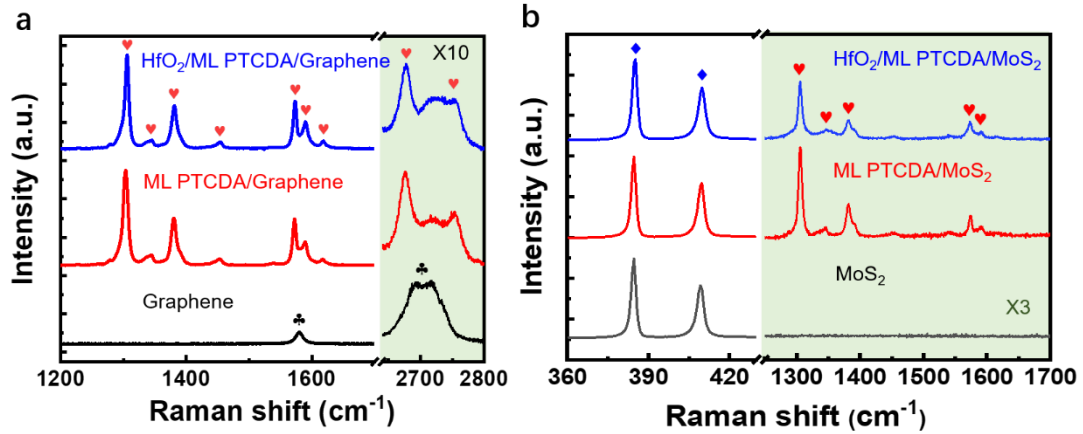
Supplementary Figure 1. AFM characterization. **a.** Left, AFM image of a multi-layer PTCDA sample on BN showing layered morphology (left). Scale bar: 4 μm . Right, height profile measured from the AFM image. The thickness of each layer is ~ 0.3 nm. **b-d.** AFM images of exfoliated 2D materials (graphene, BN, and MoS₂, respectively, left row), after ML PTCDA deposition (middle row) and after 2 nm HfO₂ deposition (right row). Scale bars: 3 μm . The height profiles after each step are shown on the right. **e.** AFM images of an exfoliated MoS₂ (left) and after 10 nm HfO₂ deposition without PTCDA (right). Scale bars: 3 μm .



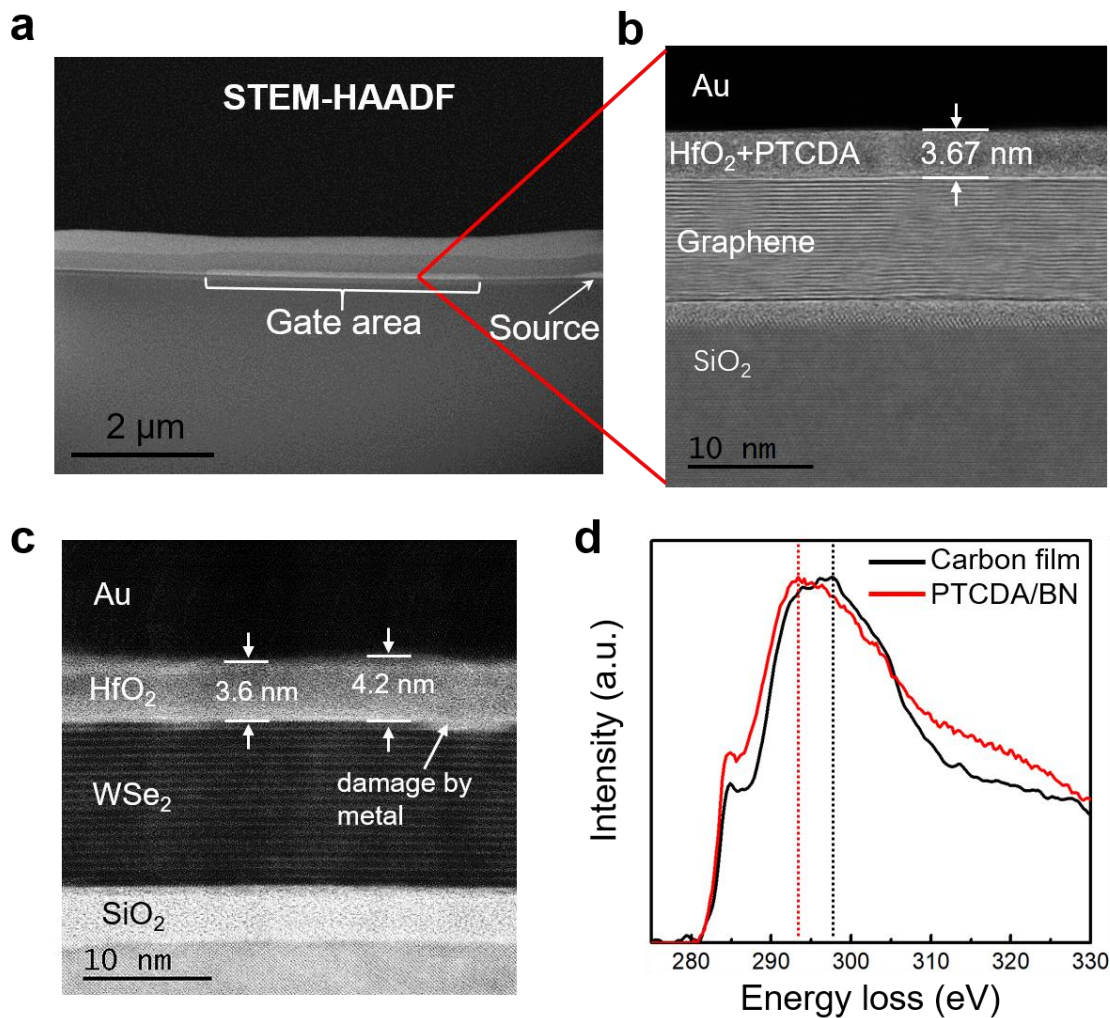
Supplementary Figure 2. Cross-polarized optical microscopy. **a.** Optical microscopic image of a ML PTCDA/graphene sample. The highlighted area is monolayer graphene. Scale bar: $5 \mu\text{m}$. **b.** Polar plots of the normalized intensity under cross-polarized optical microscope measured from **c**. **c.** Cross-polarized microscopic images of the sample at different rotation angles under 532 nm illumination. As we rotate the sample, the intensity is uniformly modulated with 180° period, which is consistent with the symmetry of PTCDA packing and confirms the single-crystalline nature of the ML PTCDA. Scale bar: $5 \mu\text{m}$.



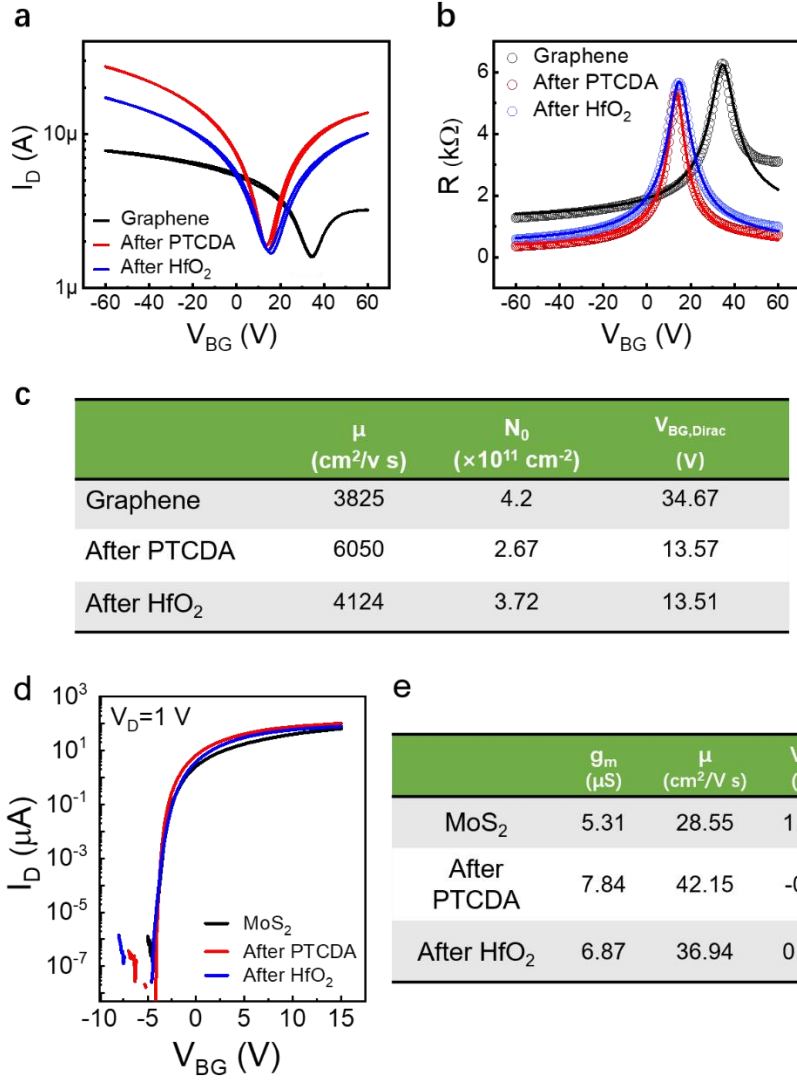
Supplementary Figure 3. Water contact angle measurement. The water contact angle of CVD graphene on Cu foil before (a) and after (b) deposition of ML PTCDA. The contact angle decreased from 95° to 62° .



Supplementary Figure 4. Raman characterization. **a.** (From bottom to top) The Raman spectrum of an exfoliated few-layer graphene, after ML PTCDA and after ALD HfO₂. **b.** (From bottom to top) The Raman spectrum of an exfoliated few-layer MoS₂, after ML PTCDA and after ALD HfO₂. Red Heart symbol represent the characteristic Raman peak of PTCDA (1305 cm⁻¹, 1345 cm⁻¹, 1381 cm⁻¹, 1573 cm⁻¹, 1590 cm⁻¹, 1618 cm⁻¹, 2686 cm⁻¹, 2757 cm⁻¹). Black Club symbol represent the characteristic Raman peak of graphene (1580 cm⁻¹, 2710 cm⁻¹). Blue Diamond symbol represent the characteristic Raman peak of MoS₂ (385 cm⁻¹, 409 cm⁻¹). We can see that in both cases, the PTCDA layer is still well preserved during ALD process.



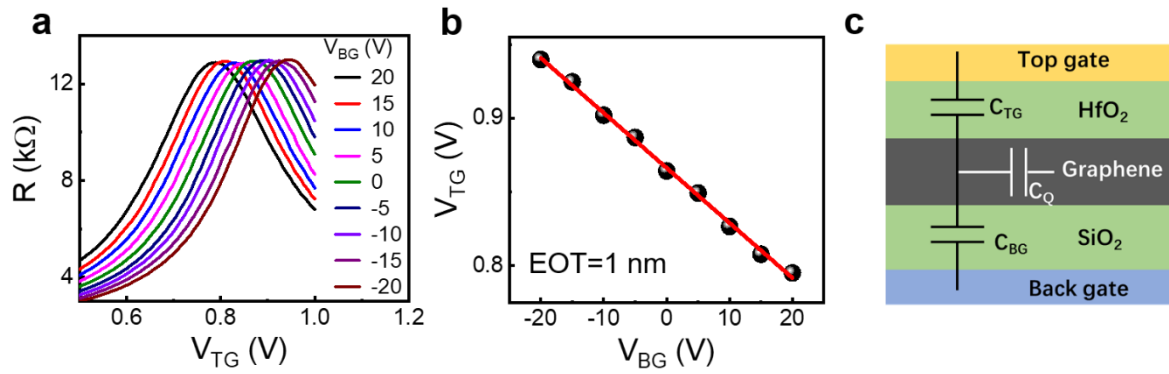
Supplementary Figure 5. Cross-sectional STEM characterization. **a-b.** Cross-sectional STEM high angle annular dark field (STEM-HAADF) at low magnification (**a**) and high-resolution STEM-BF (**b**) images of an Au/HfO₂/ML PTCDA/multi-layer graphene stack. The topgate and source metal electrodes are marked in (**a**). The thin white horizontal line across the entire image in (**a**) is the uniform deposition of ML PTCDA/HfO₂. **c.** Cross-sectional STEM-BF image of an Au/HfO₂/1 nm Al/WSe₂ stack, showing large thickness variation of 0.6 nm in HfO₂. In addition, damage of top WSe₂ layer by Al metal is evident. **d.** EELS spectra of the PTCDA grown on BN (Red) and amorphous carbon (Black) on carbon film of a TEM grid, respectively, which is consistent with the result shown in Fig. 2e.



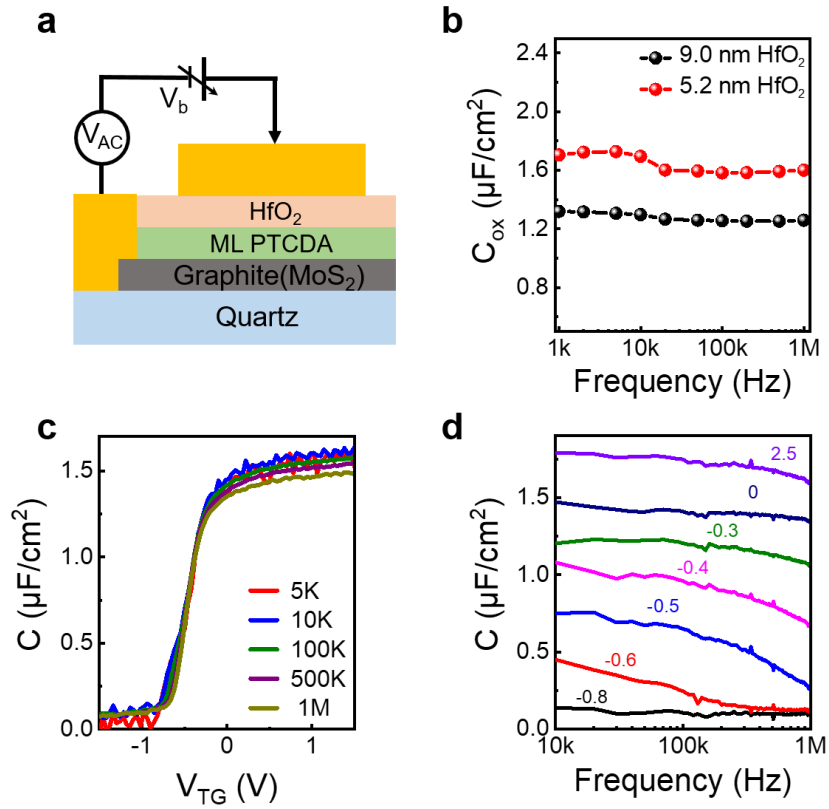
Supplementary Figure 6. Step-by-step electrical measurements of topgate FET. a. Double-sweep transfer curves of a backgate graphene FET on 275 nm SiO₂/Si substrate as fabricated, after growing ML PTCDA and after 4 nm HfO₂ ALD. $V_D=10$ mV. **b.** Experimental data (symbols) and numerical fitting (lines) of R vs. V_{BG} from (a) to derive the mobility and residual carrier density. The fitting procedure¹ is as follow: the carrier density n_{TG} in the channel can be described by the gate capacitance and the quantum capacitance. The expression is $V_{TG} - V_{TG,Dirac} = \frac{e}{C_{ox}} n_{TG} + \frac{\hbar v_F \sqrt{\pi n_{TG}}}{e}$, where C_{ox} is the gate capacitance and v_F is the Fermi velocity. The total resistance consists of the contact resistance and channel resistance and can be described by $R_{total} = R_c + R_{ch} = R_c + \frac{L/W}{\sqrt{n_0^2 + n_{TG}^2 e \mu}}$. Where L/W , μ and n_0 are

Length/Width ratio, mobility and residual carrier density induce by charged impurities, respectively. **c.** The derived mobility and residual carrier density after each step. The mobility and residual carrier density are improved and the Dirac point is closer to zero after the

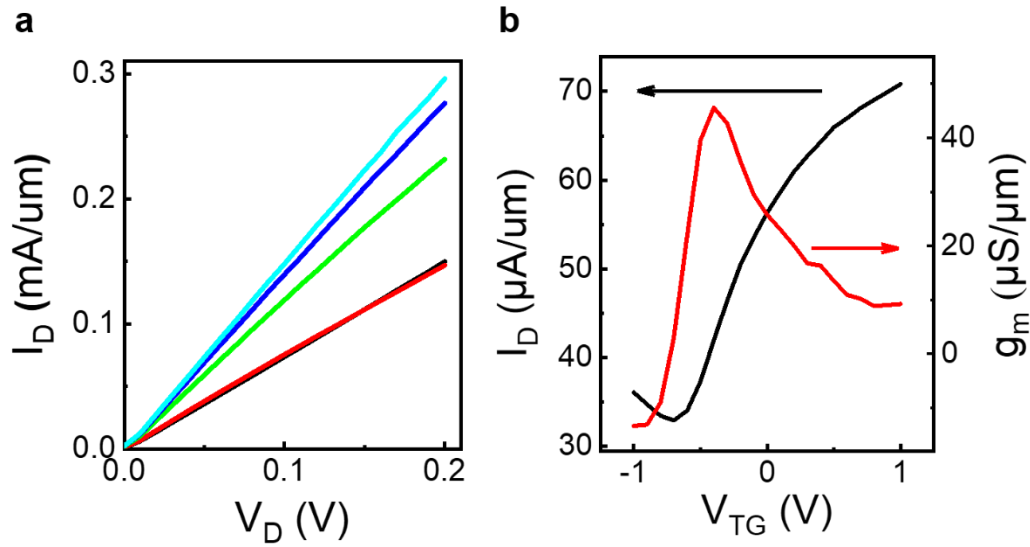
fabrication of gate stack, which show that PTCDA does not introduce defects, doping or interface states in graphene. **d.** Transfer curves of a backgate MoS₂ FET on 30 nm Al₂O₃/Si substrate as fabricated, after growing ML PTCDA and after 4 nm HfO₂ ALD. $V_D=1$ V. **e.** The derived transconductance, mobility and threshold voltage after each step.



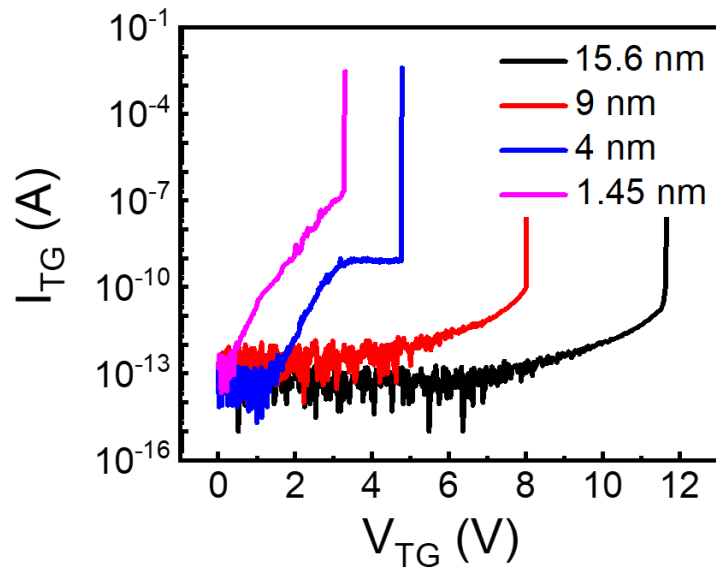
Supplementary Figure 7. Double-gate measurement to extract C_{TG} . **a.** Transfer curves of a topgate graphene FET under different V_{BG} from -20 to 20 V, $V_D=10$ mV. **b.** Dirac point voltage as a function of V_{BG} . Solid line shows linear fitting of the experiment data. The slope is -0.0036, corresponding to EOT=1 nm. **c.** A schematic view of the dual-gate model². C_{TG} is the total capacitance of HfO₂ layer/PTCDA layer, C_Q is the quantum capacitance of graphene and C_{BG} is capacitance of 275 nm SiO₂.



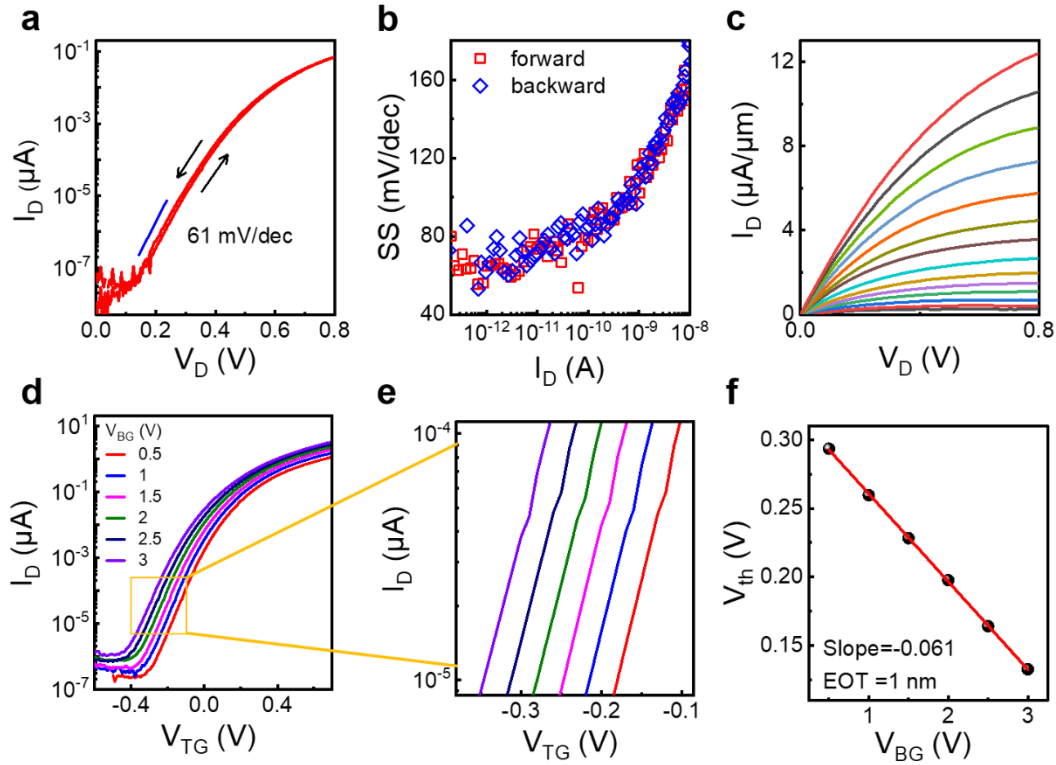
Supplementary Figure 8. Capacitance-frequency (C - f) measurement and capacitance-voltage (C - V) measurement to extract C_{TG} . **a.** Schematic of the experimental capacitor structure. **b.** Measured capacitance of HfO_2 /PTCDA stack with two different HfO_2 thickness in the frequency range of 1 kHz – 1 MHz. **c.** C - V characteristics under different frequency with 6 nm HfO_2 /MoS₂ structure on quartz substrate. **d.** C - f characteristics under different gate voltage C_{TG} (V) with the same device in **c**.



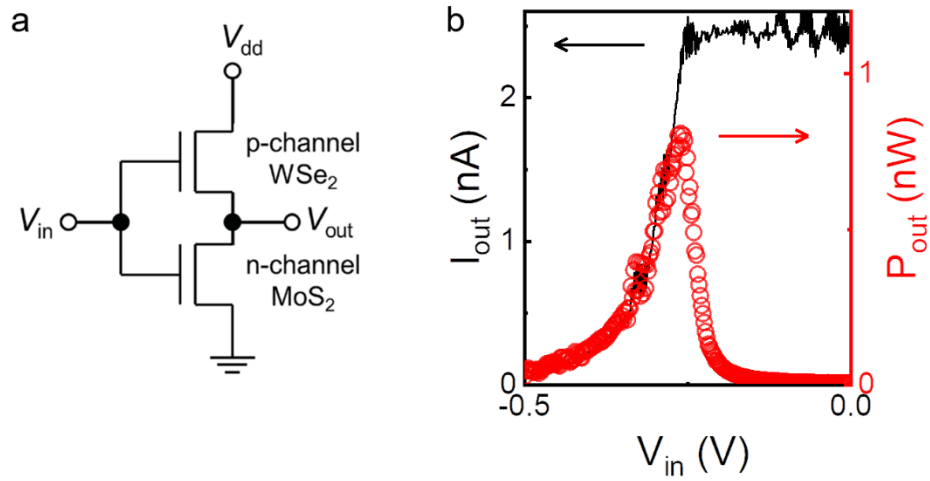
Supplementary Figure 9. DC performance of the RF graphene transistor shown in Fig. 3 of main text. a. Low bias I_D - V_D output characteristics at various gate voltages (V_{TG} from -1 to 1 V, step is 0.5 V). **b.** I_D - V_{TG} transfer characteristics and transconductance at $V_D=50$ mV.



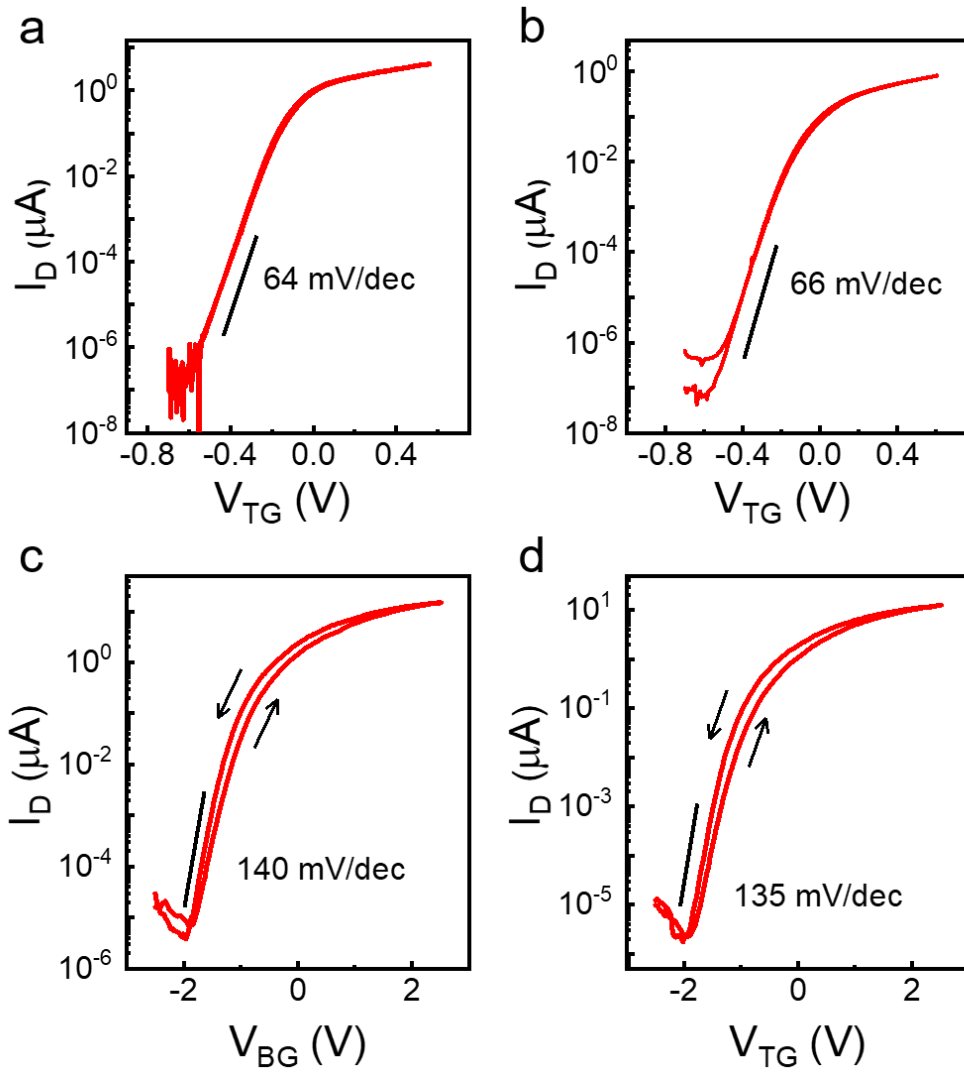
Supplementary Figure 10. Breakdown characteristics of ML PTCDA/HfO₂. Gate leakage current I_{TG} as a function of V_{TG} measured on topgate graphene FETs with different t_{ox} of 1.45 nm, 4 nm, 9 nm and 15.6 nm.



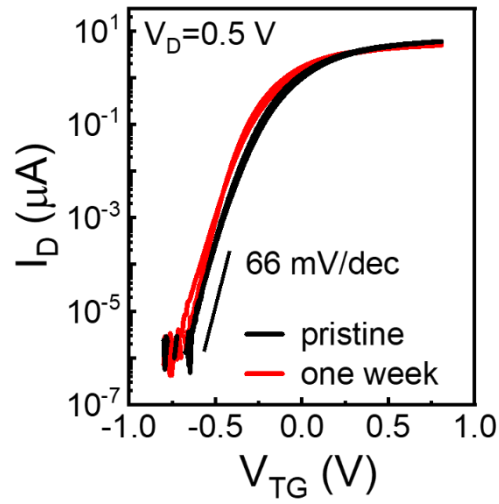
Supplementary Figure 11. Topgate MoS₂ EFT with 1 nm EOT ($t_{ox}=1.45$ nm, monolayer MoS₂). **a.** Double-sweep transfer characteristics measured under $V_D=0.1$ V and $V_{BG}=-0.5$ V, showing $SS=61$ mV/dec and no hysteresis. **b.** SS versus I_D characteristics of the device in **a**, showing constant SS across over 3 orders of I_D with minimum SS of ~ 60 mV/dec for both forward and reverse sweeping. **c.** Output characteristics of the same device under $V_{BG}=15$ V. From top to bottom, V_{TG} from 0.8 V to -0.5 V with 0.1 V step. **d.** Transfer characteristics under different V_{BG} from 0.5 V to 3 V with 0.5 V step. **e.** Magnification of the transfer curves from **d**. **f.** The threshold voltage V_{th} as the function of V_{BG} . From the linear fitting, EOT=1 nm is obtained.



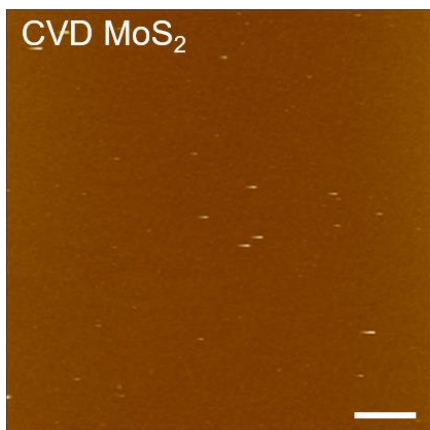
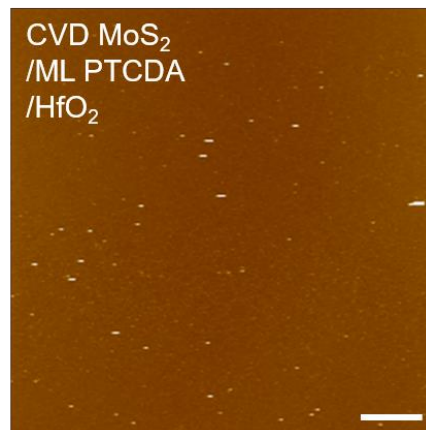
Supplementary Figure 12. Ultra-low power CMOS inverter. **a.** The equivalent circuit diagram. WSe_2 is used in a p-channel transistor and MoS_2 is used in a n-channel transistor, which are then connected in series to construct a CMOS inverter. **b.** Measured operating current I_{dd} and Power P_{out} as function of V_{in} at $V_{dd}=0.5$ V.



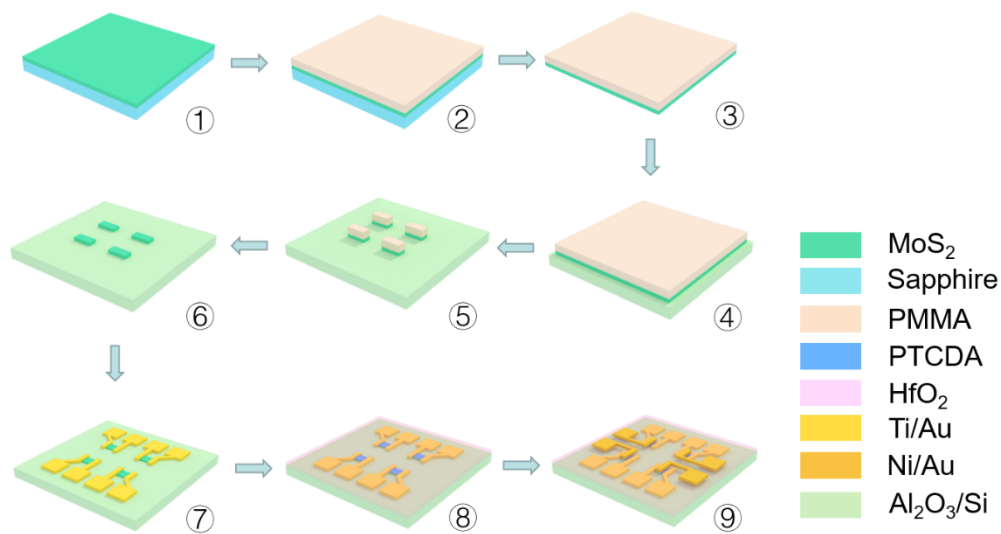
Supplementary Figure 13. Hysteresis of topgate MoS_2 FET. **a-b.** Double-sweep transfer characteristics of two typical FETs based on exfoliated MoS_2 samples measured under $V_D=0.5$ V with negligible hysteresis (<10 mV). **c-d.** Double-sweep transfer characteristics of two typical FETs based on CVD MoS_2 samples measured under $V_D=0.1$ V, showing slight hysteresis (~ 100 mV) which may be induced by PMMA residual during transfer processes.



Supplementary Figure 14. Long-term stability. Transfer curves of topgate MoS₂ transistor with 4 nm HfO₂ as gate dielectric. The black line and red line show the results from the same device after fabrication and after one-week storage, respectively.

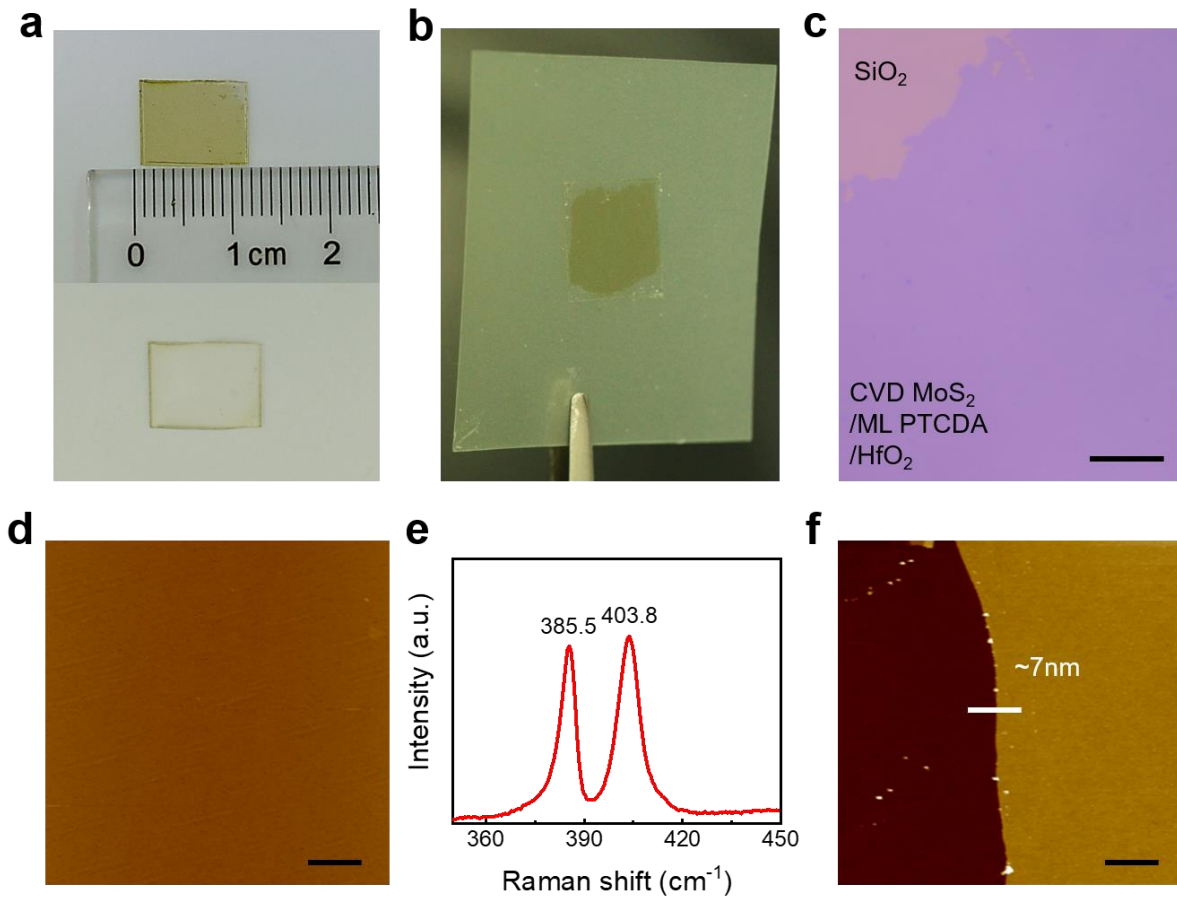
a**b**

Supplementary Figure 15. AFM characterization of CVD MoS₂ film. AFM images of transferred CVD MoS₂ film before (a) and after (b) depositing ML PTCDA/6 nm HfO₂. Roughness are 0.2 nm and 0.3 nm respectively. Scale bars: 3 μm.

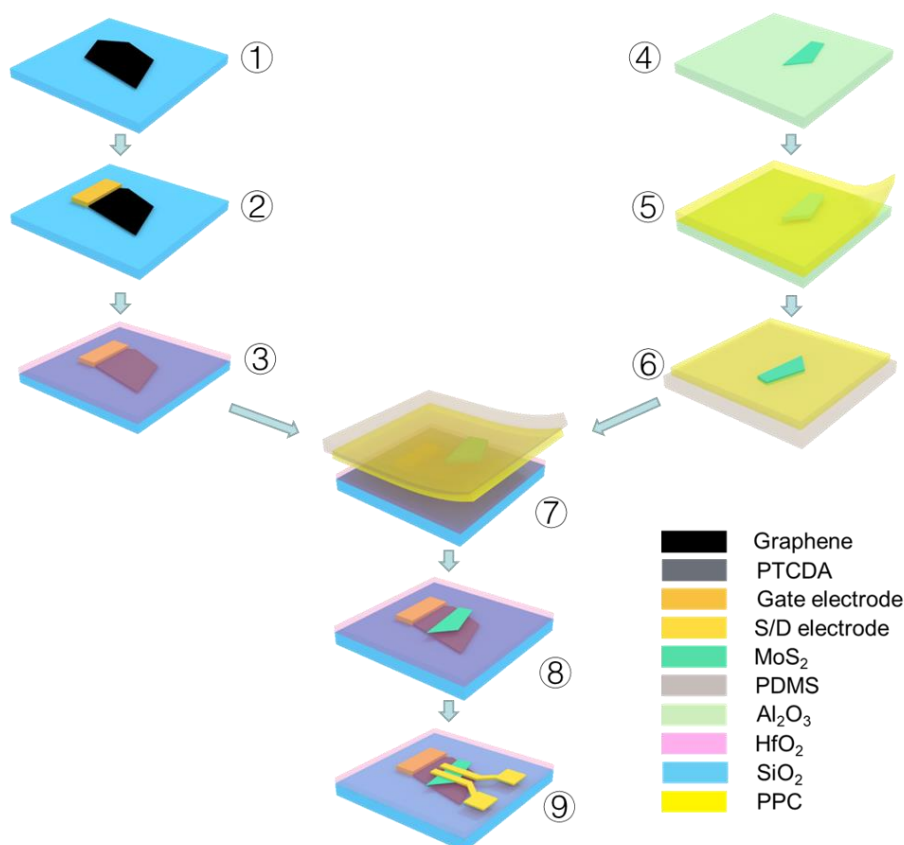


Supplementary Figure 16. Fabrication process of topgate FET array on CVD MoS₂

- ① CVD growth of monolayer MoS₂ film on sapphire.
- ② Spin coat PMMA as a transfer support layer.
- ③ Use 30% NaOH solution to etch the sapphire substrate until PMMA/MoS₂ layer separating from sapphire substrate.
- ④ After several times of deionized water cleaning, the PMMA/MoS₂ layer was transferred to 30 nm Al₂O₃/Si.
- ⑤ Pattern the channel regions on MoS₂ film by electron beam lithography (EBL) and CF₄ plasma etching.
- ⑥ Remove PMMA using acetone.
- ⑦ Pattern source/drain electrodes by EBL and deposit 10 nm Ti/50 nm Au by e-beam evaporation (EBE), then lift off.
- ⑧ Deposit ML PTCDA and 6 nm HfO₂.
- ⑨ Pattern topgate electrodes by EBL, deposition of 5 nm Ti/15 nm Au by EBE and lift off.

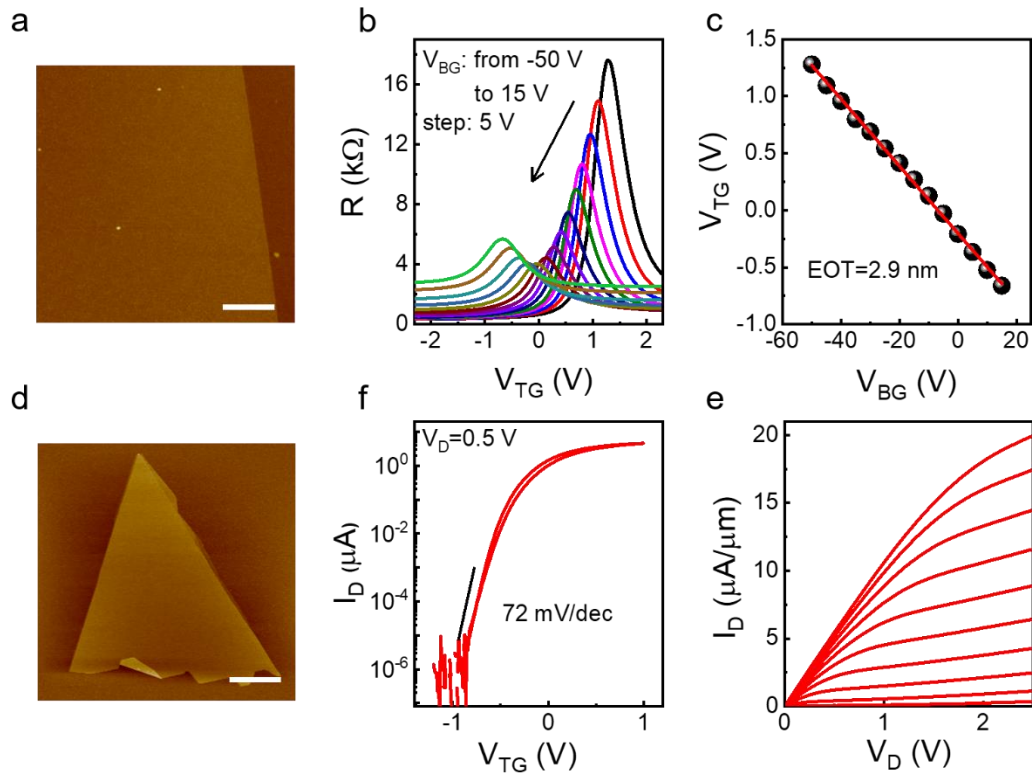


Supplementary Figure 17. Transfer of CVD MoS₂ using ML PTCDA/HfO₂ stack as support layer. **a.** Top image shows HfO₂/ML PTCDA deposited on centimeter MoS₂ film which is grown on sapphire. The bottom image shows sapphire substrate after transfer. Changes in color and transparency indicate that the CVD MoS₂ film has been successfully transferred. **b.** Photograph of CVD MoS₂ film/ML PTCDA/HfO₂ stack attached to thermal release tape during the transfer process. **c.** Optical microscope image of CVD MoS₂ film/ML PTCDA/HfO₂ stack transferred onto SiO₂/Si substrate. Scale bar is 200 μm . **d.** AFM image of the transferred film on SiO₂. Scale bar is 4 μm . **e.** Raman spectrum of the transferred film showing characteristic peak of monolayer MoS₂ film at 385.5 cm^{-1} and 403.8 cm^{-1} . **f.** AFM image on the edge of the transferred film, showing ultra-clean surface and small roughness. We deposited 6nm HfO₂, so the total height of the MoS₂/ML PTCDA/HfO₂ stack is about $\sim 7\text{nm}$. Scale bar is 2 μm .



Supplementary Figure 18. Fabrication process of short-channel MoS₂ FET

- ① Exfoliate few-layer graphene on 275 nm SiO₂/Si substrate.
- ② Deposit Au electrode to cover a small portion of graphene as gate electrode.
- ③ Deposit ML PTCDA/HfO₂ on graphene as gate dielectric.
- ④ Exfoliate bi-layer MoS₂ flake on 30 nm Al₂O₃/Si substrate.
- ⑤ Spin coat pole-propylene carbonate (PPC) (Sigma-Aldrich, CAS 25511-85-7) layer on MoS₂.
- ⑥ The PPC/MoS₂ flake layer was peeled from the Al₂O₃/Si substrate and placed onto a transparent elastomer stamp (poly dimethyl siloxane, PDMS) for transfer.
- ⑦ The MoS₂ was transferred on the top of gate stack using a micro-manipulator under microscope.
- ⑧ Remove PPC with acetone.
- ⑨ Pattern source/drain electrodes by EBL and deposit 1 nm Ti/10 nm Pd by EBE, then lift off.



Supplementary Figure 19. Topgate FETs with Al₂O₃ dielectric. **a.** AFM image of 4 nm Al₂O₃/ML PTCDA/graphene structure on 100 nm SiO₂/Si substrate with roughness of ~150 pm. Scale bar is 2 μm. **b.** Transfer curves of a topgate bi-layer graphene FET ($t_{ox}=4$ nm) under different V_{BG} from -50 to 15 V, $V_D=10$ mV. **c.** Dirac point as a function of V_{BG} . Solid line shows linear fitting of the experiment data with slope of -0.029, corresponding to EOT=2.9 nm. **d.** AFM image of 4 nm Al₂O₃/ML PTCDA/MoS₂ structure on 30 nm Al₂O₃/Si substrate with roughness of ~150 pm. Scale bar is 3 μm. **e.** Double-sweep transfer characteristics of MoS₂ FET ($t_{ox}=4.5$ nm) measured under $V_D=0.1$ V, showing SS=72 mV/dec and negligible hysteresis. **f.** Output characteristics of the same device under $V_{BG}=15$ V. From top to bottom, V_{TG} from 1.4 V to -0.6 V with 0.2 V step.

Supplementary Table 1. Comparison of ALD oxide properties on graphene

Dielectric layer	Modified method	Thickness of seed layer (nm)	Roughness (nm)	t_{ox} (nm)	Gate capacitance ($\mu\text{F}/\text{cm}^2$)	EOT (nm)	Ref.
HfO ₂	NFC polymer	10		20	0.18	19	3
Al ₂ O ₃	O ₂ plasma	1	0.37	5	0.78	4.42	4
HfO ₂	PTCDA	0.3-0.6	0.8-1.1	10	0.89	3.87	5
Al ₂ O ₃	Ozone			4.5	0.92	3.74	6
Y ₂ O ₃	Y seed layer	1	0.3	6	1.16	2.97	7
HfO ₂	Hf seed layer	3	0.88	5	2.5	1.38	8
HfO ₂	Electron beam irradiation		0.4	4	2.63	1.3	9
HfO₂	ML PTCDA	0.3	0.13	1.5	3.45	1	this work

Supplementary Table 2. Comparison of ALD oxide properties on TMDs

Gate methods	Dielectric layer	EOT (nm)	Roughness (nm)	Channel length(nm)	SS (mV/dec)	Ref.
Directly ALD	30 nm HfO ₂			long channel	75	10
Ozone pretreatment	6 nm HfO ₂	3.55			75	11
Remote oxygen plasma pretreatment	6.6 nm Al ₂ O ₃		0.58		101	12
Plasma pretreatment	6.1 nm Al ₂ O ₃	3.55			85	13
Deposit Y, and oxidize as seed layer	3-7 nm Y ₂ O ₃ + 9 nm HfO ₂	4.42			65	14
PEALD	4 nm HfO ₂		0.3		~ 130	15
AlN as seed layer	1 nm AlN+ 5 nm Al ₂ O ₃		0.63		~ 120	16
ML PTCDA as seed layer	1.5 nm HfO₂	1	0.13		60	this work
1L TiOPc as seed layer (WSe ₂)	5.3 nm Al ₂ O ₃	3	0.15		80	17
Directly ALD ZrO ₂ (WSe ₂)	17.5 nmZrO ₂	5.46			60	18
ML PTCDA as seed layer (WSe₂)	2.8 nm HfO₂	1.3	0.13	67	this work	
Transfer Al ₂ O ₃ /Al nanowires	5 nm Al ₂ O ₃	2.5		30	80	19
Directly ALD	10 nm HfO ₂			15	205	20
Deposit Ti, and oxidize as seed layer	4 nm HfO ₂ /1.2 nm TiO ₂		0.4	14	86.5	21
Directly ALD on Pt/Ti gate electrode	7.5 nm HfO ₂	2.5		10	200	22
Transfer Al ₂ O ₃ /Al nanowires	5 nm Al ₂ O ₃	2.5		10	250	19
Transfer h-BN as gate dielectric layer	4 nm BN			9	93	23
Transfer h-BN as gate dielectric layer	2.5 nm BN			4	208	23
Directly ALD on SWCNT gate electrode	5.8 nm ZrO ₂			1	65	24
ML PTCDA as seed layer	6 nm HfO₂	2	0.13	20	73	this work

Note: the channel material is MoS₂ unless otherwise stated.

References:

1. Kim, S. et al. Realization of a high mobility dual-gated graphene field-effect transistor with Al₂O₃ dielectric. *Appl. Phys. Lett.* **94**, 62107 (2009).
2. Xu, H., et al., Quantum capacitance limited vertical scaling of graphene field-effect transistor. *ACS Nano* **5**, 2340-2347 (2011).
3. Farmer, D.B. et al. Utilization of a Buffered Dielectric to Achieve High Field-Effect Carrier Mobility in Graphene Transistors. *Nano Lett.* **9**, 4474-4478 (2009).
4. Nourbakhsh, A. et al. Graphene oxide monolayers as atomically thin seeding layers for atomic layer deposition of metal oxides. *Nanoscale* **7**, 10781-10789 (2015).
5. Sangwan, V.K. et al. Quantitatively Enhanced Reliability and Uniformity of High- κ Dielectrics on Graphene Enabled by Self-Assembled Seeding Layers. *Nano Lett.* **13**, 1162-1167 (2013).
6. Jandhyala, S. et al. Atomic Layer Deposition of Dielectrics on Graphene Using Reversibly Physisorbed Ozone. *ACS Nano* **6**, 2722-2730 (2012).
7. Takahashi, N. & Nagashio, K. Buffer layer engineering on graphene via various oxidation methods for atomic layer deposition. *Appl. Phys. Express* **9**, 125101 (2016).
8. Jeong, S. et al. Thickness scaling of atomic-layer-deposited HfO₂ films and their application to wafer-scale graphene tunnelling transistors. *Sci. Rep.* **6** 20907 (2016).
9. Xiao, M., Qiu, C., Zhang, Z. & Peng, L. Atomic-Layer-Deposition Growth of an Ultrathin HfO₂ Film on Graphene. *ACS Appl. Mater. Inter.* **9**, 34050-34056 (2017).
10. Radisavljevic, B., Radenovic, A., Brivio, J., Giacometti, V. & Kis, A. Single-layer MoS₂ transistors. *Nat. Nanotechnol.* **6**, 147-150 (2011).
11. Wang, J. et al. Integration of High- κ Oxide on MoS₂ by Using Ozone Pretreatment for High-Performance MoS₂ Top-Gated Transistor with Thickness-Dependent Carrier Scattering Investigation. *Small* **11**, 5932-5938 (2015).
12. Liu, H., Xu, K., Zhang, X. & Ye, P.D. The integration of high- κ dielectric on two-dimensional crystals by atomic layer deposition. *Appl. Phys. Lett.* **100**, 152115 (2012).
13. Yang, J. et al. Improved Growth Behavior of Atomic-Layer-Deposited High- κ Dielectrics on Multilayer MoS₂ by Oxygen Plasma Pretreatment. *ACS Appl. Mater. Inter.* **5**, 4739-4744 (2013).
14. Zou, X. et al. Interface Engineering for High-Performance Top-Gated MoS₂ Field-Effect Transistors. *Adv. Mater.* **26**, 6255-6261 (2014).
15. Price, K.M., Schauble, K.E., McGuire, F.A., Farmer, D.B. & Franklin, A.D. Uniform Growth of Sub-5-Nanometer High- κ Dielectrics on MoS₂ Using Plasma-Enhanced Atomic Layer Deposition.

- ACS Appl. Mater. Inter.* **9**, 23072-23080 (2017).
16. Qian, Q. et al. Improved Gate Dielectric Deposition and Enhanced Electrical Stability for Single-Layer MoS₂ MOSFET with an AlN Interfacial Layer. *Sci. Rep.* **6**, 27676 (2016).
 17. Park, J.H. et al. Atomic Layer Deposition of Al₂O₃ on WSe₂ Functionalized by Titanyl Phthalocyanine. *ACS Nano* **10**, 6888-6896 (2016).
 18. Fang, H. et al. High-performance single layered WSe₂ p-FETs with chemically doped contacts. *Nano Lett.* **12**, 3788-3792 (2012).
 19. English, Chris D., et al. Approaching ballistic transport in monolayer MoS₂ transistors with self-aligned 10 nm top gates. *Inter. Electron Dev. Meet. Tech. Digest* 5.6.1-5.6.4 (2016).
 20. Nourbakhsh, A. et al. 15-nm channel length MoS₂ FETs with single-and double-gate structures. *Symp. VLSI Tech.* 28-29 (2015).
 21. Zhu, Y. et al. Monolayer Molybdenum Disulfide Transistors with Single-Atom-Thick Gates. *Nano Lett.* **18**, 3807-3813 (2018).
 22. Yang, L., et al. 10 nm nominal channel length MoS₂ FETs with EOT 2.5 nm and 0.52 mA/μm drain current. *73rd Annual Device Research Conference. IEEE*, 237-238(2015).
 23. Xie, L. et al. Graphene-Contacted Ultrashort Channel Monolayer MoS₂ Transistors. *Adv. Mater.* **29**, 1702522 (2017).
 24. Desai, S.B. et al. MoS₂ transistors with 1-nanometer gate lengths. *Science* **354**, 99-102 (2016).